Analytic high-order energy derivatives for metal nanoparticle-mediated infrared and Raman scattering spectra within the framework of quantum mechanics/molecular mechanics model with induced charges and dipoles

Cite as: J. Chem. Phys. 157, 164110 (2022); doi: 10.1063/5.0118205 Submitted: 4 August 2022 • Accepted: 30 September 2022 • **Published Online: 27 October 2022**







Zheng Pei,¹ Yuezhi Mao,^{2,a)} D Yihan Shao,^{3,b)} and WanZhen Liang^{1,c)}







AFFILIATIONS

- 1 State Key Laboratory of Physical Chemistry of Solid Surfaces, Collaborative Innovation Center of Chemistry for Energy Materials, Fujian Provincial Key Laboratory of Theoretical and Computational Chemistry, and Department of Chemistry, College of Chemistry and Chemical Engineering, Xiamen University, Xiamen 361005, People's Republic of China
- Department of Chemistry, Stanford University, Stanford, California 94305, USA
- Department of Chemistry and Biochemistry, University of Oklahoma, Norman, Oklahoma 73019, USA
- a) Electronic mail: yuezhi.mao@stanford.edu
- b) Electronic mail: yihan.shao@ou.edu
- ^{c)}Author to whom correspondence should be addressed: liangwz@xmu.edu.cn

ABSTRACT

This work is devoted to deriving and implementing analytic second- and third-order energy derivatives with respect to the nuclear coordinates and external electric field within the framework of the hybrid quantum mechanics/molecular mechanics method with induced charges and dipoles (QM/DIM). Using these analytic energy derivatives, one can efficiently compute the harmonic vibrational frequencies, infrared (IR) and Raman scattering (RS) spectra of the molecule in the proximity of noble metal clusters/nanoparticles. The validity and accuracy of these analytic implementations are demonstrated by the comparison of results obtained by the finite-difference method and the analytic approaches and by the full QM and QM/DIM calculations. The complexes formed by pyridine and two sizes of gold clusters (Au₁₈ and Au₃₂) at varying intersystem distances of 3, 4, and 5 Å are used as the test systems, and Raman spectra of 4,4'-bipyridine in the proximity of Au₂₀₅₇ and Ag₂₀₅₇ metal nanoparticles (MNP) are calculated by the QM/DIM method and compared with experimental results as well. We find that the QM/DIM model can well reproduce the IR spectra obtained from full QM calculations for all the configurations, while although it properly enhances some of the vibrational modes, it artificially overestimates RS spectral intensities of several modes for the systems with very short intersystem distance. We show that this could be improved, however, by incorporating the hyperpolarizability of the gold metal cluster in the evaluation of RS intensities. Additionally, we address the potential impact of charge migration between the adsorbate and MNPs.

Published under an exclusive license by AIP Publishing. https://doi.org/10.1063/5.0118205

I. INTRODUCTION

In the last several decades, plasmonic metal nanoparticles (MNPs) have generated a great amount of interest due to the dramatic effect of surface localized plasmon resonance.¹⁻

Currently, plasmonic MNPs have been widely used to control and manipulate light at the nanoscale, thus regulating the photophysical and photochemical properties of molecules in their vicinity, such as enhancing molecular optical signals (absorption,⁵ Raman,^{6,7} and fluorescence⁸⁻¹⁰) and mediating molecular photochemical reactions. ^{11–14} Meanwhile, many theoretical and computational methods were developed to unravel the detailed mechanisms of molecular spectral enhancements ¹⁵ and plasmon-mediated chemical reactions ^{16,17} as well as plasmon-enhanced resonance energy transfer. ^{18–21} In many cases, the plasmon enhancement arises mainly from the electromagnetic mechanism, where an external electric field can be substantially magnified by an MNP around its surface. Accordingly, several classical nonatomistic methods ²² had been widely applied.

The hybrid MNP-molecular systems represent a challenge for theoretical and computational methods because the constituents cannot be treated on the same footing by the state-of-the-art methods. The properties of molecules require a quantum mechanics (QM) description, thanks to the high accuracy of QM methods.^{23,24} However, QM methods are unable to describe the medium to largesized MNPs due to their steep computational cost. Two kinds of simplified treatments have been usually adopted. One is to simplify the problem by assuming the molecules bonded to very small metal clusters.^{25–32} With this treatment, the optical properties of molecule-metal cluster systems can be described by the QM methods. Small MNPs, however, do not support the bulk plasmon. The other is to adopt the mixed quantum/classical approach, which combines the QM approaches with classical mechanics or electrodynamics, such as the Mie theory,³³ discrete dipole approximation,³⁴ finite difference time domain,⁵ and polarizable continuum models.35-3

To more accurately capture the plasmonic effect from MNPs with different sizes, shapes, and compositions, however, atomistic modeling of the MNP-adsorbate system is needed. Specifically, to account for the large polarizability of MNPs, (induced) charges, dipoles, and/or even multipoles would be introduced at each atom site, leading to several (polarizable) force field models for MNPs. These molecular mechanics (MM) methods include the point-dipole interaction model^{38,39} (including its combination with either electronegativity equalization⁴⁰ or charge-transfer⁴¹), charge-dipole interaction model, ^{42,43} discrete interaction model (DIM)^{44,45} and its coordination-dependent variant (cd-DIM), ⁴⁶ and atomic dipole approximation model. ⁴⁷

These MM models can be employed in combined quantum mechanics/molecular mechanics (QM/MM) modeling of probe-MNP complexes, where the probe molecule constitutes the QM region so that its vibrational motions [in infrared (IR) and Raman spectroscopy] or electronic transitions (in fluorescence) are treated using ab initio QM theories. Mikkelsen et al. have investigated the hyperpolarizability changes in organic molecules near gold nanoparticles by a polarizable QM/MM approach recently. 48 The DIM model with induced charges and induced dipoles at each metal atom, in particular, has been combined with QM methods by Jensen et al. 50-54 to model MNP-mediated one-photon 51,55 and twophoton absorption,⁵⁶ Raman,^{52,57–59} and fluorescence spectra.⁶⁰ In parallel to the QM/MM study of MNP-enhanced electronic transitions, Giovannini et al. have combined density functional theory (DFT) and time-dependent density functional theory (TDDFT) with their FQF μ models for water molecules, which are also based on fluctuating charges and induced dipoles.^{61,62}

Analytic energy derivatives can provide computational advantages in molecular geometry optimizations, vibrational frequency calculations, and molecular property descriptions.⁶³ The analytic

Raman intensities of the QM method have been derived and implemented decades ago. ^{64–66} Recently, the implementations of analytic Hessian and high-order molecular properties (such as IR and Raman intensities) have been extended to several hybrid (polarizable) QM/MM schemes for solvents or protein systems. ^{67–69} Here, inspired by the encouraging results of the QM/DIM model from Jensen *et al.*, ^{50–52} we present our implementation of this model and its analytic energy derivatives with respect to the nuclear coordinates and perturbed electric field for the study of the adsorbate–MNP systems. Compared to earlier implementations of IR and Raman intensities within a polarizable QM/MM model, ^{67–69} our implementation is applicable to polarizable force fields involving both induced charges and dipoles, such as the DIM model for metal clusters.

The paper is organized as follows: Sec. II briefly recaps the basic theoretical foundation of the polarizable QM/MM model for the ground-state energy of a molecule–MNP system and presents the analytical expressions for high-order derivatives of the energy with respect to the QM nuclear and field perturbations. It is followed by the computational details in Sec. III. In Sec. IV, using the pyridine molecule in the vicinity of three gold clusters as testing systems, the computed IR and Raman spectra are presented and discussed. In addition, the MNP-mediated Raman spectra of 4,4′-bipyridine on gold and silver MNPs are simulated by the QM/DIM method and compared with experimental spectra. Moreover, the effects of nonlinear response of MNP and charge migration to Raman intensity are analyzed. Finally, the concluding remarks and potential future improvements are summarized in Sec. V.

II. THEORY

A. Total energy of hybrid QM/MM system

Here, the DIM method is briefly described with a compact notation, and the reader is referred to the original publications. ^{44,45} The energy of the MM region is given by the electrostatic interaction,

$$E^{\text{MM}} = \frac{1}{2} \mathcal{M}^{\text{ind}} \cdot \mathcal{F} \cdot \mathcal{M}^{\text{ind}} - \mathcal{M}^{\text{ind}} \cdot \mathcal{F}^{\text{tot}}, \tag{1}$$

where \mathcal{M}^{ind} represents the collection of induced charges and dipoles $(q^{\text{ind}}, \vec{\mu}^{\text{ind}})$ on MM atoms; \mathcal{T} represents the interaction matrices of charge-charge, charge-dipole, and dipole-dipole $(T^{(0)}, T^{(1)}, T^{(2)})$ as

$$T_{ij}^{(0)} = \frac{1}{r_{ij}} \operatorname{erf}\left(\frac{r_{ij}}{\sigma}\right), \qquad T_{ij}^{(n)} = (-\nabla_j)^n T_{ij}^{(0)},$$
 (2)

where r_{ij} is the distance between the ith and jth MM atoms and σ is the width of Gaussian functions used to damp the electrostatic interaction between neighboring atoms. ⁴⁴ The diagonal block of \mathcal{T} is formed by the atomic capacitance (c_i) and polarizability (α_i) for charge and dipole self-interactions at ith MM atom, respectively. \mathcal{F} tot is the total external generalized field exerted on the MM sites, including both potentials and fields $(-V, \vec{E})$. Using the variational condition, the stationary solution is given by solving a linear equation,

$$\begin{pmatrix} \mathcal{F} & \mathbf{1}^{\prime T} \\ \mathbf{1}^{\prime} & 0 \end{pmatrix} \begin{pmatrix} \mathcal{M}^{\text{ind}} \\ \lambda \end{pmatrix} = \begin{pmatrix} \mathcal{F}^{\text{tot}} \\ Q \end{pmatrix}, \tag{3}$$

where the Lagrangian multiplier λ is introduced to constrain the net charge for the MM region as Q. $\mathbf{1}'$ refers to a row vector $(1,0,0,0,1,0,0,0,\dots)$ with a value of 1 for only the induced charge on each MM atom. When Q is equal to 0 (as for all test cases in this work), the solution to Eq. (3) could be formally written as

$$\mathcal{M}^{\text{ind}} = \mathcal{T}^{-1} \cdot \mathcal{F}^{\text{tot}}, \tag{4}$$

where \mathcal{T}^{-1} represents the upper-left $4N_{\rm MM} \times 4N_{\rm MM}$ block of the inverse of the matrix in Eq. (3). Therefore, the MM energy is reformulated as

$$\begin{split} E^{\text{MM}} &= -\frac{1}{2} \mathcal{M}^{\text{ind}} \cdot \mathcal{F}^{\text{tot}} = -\frac{1}{2} \mathcal{M}^{\text{ind}} \cdot \mathcal{T} \cdot \mathcal{M}^{\text{ind}} \\ &= -\frac{1}{2} \mathcal{F}^{\text{tot}} \cdot \mathcal{T}^{-1} \cdot \mathcal{F}^{\text{tot}}. \end{split} \tag{5}$$

The last expression for the MM energy will be used in the derivation of the high-order derivatives of the energy.

When the MM region is adjacent to the QM region (as described on the DFT level of theory), the total generalized field \mathcal{F}^{tot} would include the contributions from the QM region in addition to the external source,

$$\mathcal{F}^{\text{tot}} = \mathcal{F}^{\text{QM}} + \mathcal{F}^{\text{ext}}$$

$$= -\mathbf{V} \cdot \mathbf{P} + \sum_{I} Z_{I} \mathcal{T}_{I} + \mathcal{R} \vec{f}^{\text{ext}}, \qquad (6)$$

where the matrix **V** contains integrals $\langle \phi_{\mu} | \mathcal{T} | \phi_{\nu} \rangle$. Namely, for each pair of the basis function $(\phi_{\mu}$ and $\phi_{\nu})$ and the *j*th MM atom, it contains the interaction between the basis function pair and a Gaussian MM charge (with width σ'),

$$V_{j,\mu\nu}^{(0)} = \langle \phi_{\mu} | \frac{1}{|\vec{r} - \vec{R}_{i}'|} \operatorname{erf}\left(\frac{|\vec{r} - \vec{R}_{i}'|}{\sigma'}\right) | \phi_{\nu} \rangle, \tag{7}$$

and its first derivatives,

$$V_{j,\mu\nu}^{(1)} = -\nabla_j \left(\langle \phi_{\mu} | \frac{1}{|\vec{r} - \vec{R}_j'|} \operatorname{erf} \left(\frac{|\vec{r} - \vec{R}_j'|}{\sigma'} \right) | \phi_{\nu} \rangle \right). \tag{8}$$

In Eq. (6), **P** is the density matrix with elements $P^{\mu\nu}$, Z_I labels the Ith QM nuclear charge, \mathcal{T}_I is the corresponding generalized external field on MM atoms, and $\mathcal{R}\vec{f}^{\text{ext}}$ represents the generalized field on each MM atom at position $(R'_{ix}, R'_{iy}, R'_{iz})$,

$$\mathcal{R}\vec{f}^{\text{ ext}} = \begin{pmatrix} R'_{1x} & R'_{1y} & R'_{1z} \\ 1 & 0 & 0 \\ 0 & 1 & 0 \\ 0 & 0 & 1 \\ R'_{2x} & R'_{2y} & R'_{2z} \\ 1 & 0 & 0 \\ 0 & 1 & 0 \\ 0 & 0 & 1 \\ \dots & \dots & \dots \end{pmatrix} \begin{pmatrix} f_{x}^{\text{ext}} \\ f_{y}^{\text{ext}} \\ f_{z}^{\text{ext}} \end{pmatrix}. \tag{9}$$

With the definition of the total generalized field \mathcal{F}^{tot} in Eq. (6), the total electronic energy of the system can then be expressed as

$$E = \mathbf{P} \cdot \left(\mathbf{h}_0 + \frac{1}{2} \mathbf{H} \cdot \mathbf{P} \right) + E_{xc} - \vec{\mu}^{\text{QM}} \cdot \vec{f}^{\text{ext}}$$
$$- \frac{1}{2} \mathcal{M}^{\text{ind}} \cdot \mathcal{F}^{\text{tot}} + E_{\text{vdW}}^{\text{QM/MM}}, \tag{10}$$

where the first term is the well-known DFT core Hamiltonian \mathbf{h}_0 and the two-electron integral supermatrix II in atomic basis $(\phi_u, \phi_v, \phi_\lambda, \phi_\sigma)$ is

$$\Pi_{\mu\nu,\lambda\sigma} = (\mu\nu|\lambda\sigma) - C_{\rm HFX}(\mu\lambda|f(\vec{r}_{12})|\nu\sigma), \tag{11}$$

adopting approximate coefficient $C_{\rm HFX}$ and operator $f(\vec{r}_{12})$ for hybrid and range-separated functionals. Furthermore, $E_{\rm xc} = \int {\rm d}\vec{r} f_{\rm xc}(\vec{r})$ is the DFT exchange-correction energy, and $\vec{\mu}^{\rm QM}$ is the dipole moment of the QM region,

$$\vec{\mu}^{\text{QM}} = -\mathbf{P} \cdot \vec{\mathbf{M}} + \sum_{I} Z_{I} \vec{R}_{I}, \tag{12}$$

which leads to the interaction between QM and external fields within the dipole approximation. Here, $\vec{\mathbf{M}}$ is the dipole moment matrix and \vec{R}_I the Ith QM nuclear coordinate. The corresponding Fock matrix to be used in the self-consistent field (SCF) cycles could be obtained by differentiating the total energy given by Eq. (10) with respect to the density matrix (\mathbf{P}),

$$\mathbf{F} = \mathbf{h}_0 + \mathbf{M} \cdot \mathbf{f}^{\text{ext}} + \mathcal{M}^{\text{ind}} \cdot \mathbf{V} + \mathbf{II} \cdot \mathbf{P} + \mathbf{F}_{xc}, \tag{13}$$

where the elements of \mathbf{F}_{xc} can be computed as

$$(F_{xc})_{\mu\nu} = \int d\vec{r} \sum_{\mathcal{F}} \frac{\partial f_{xc}}{\partial \xi} \frac{\partial \xi}{\partial P^{\mu\nu}},$$
 (14)

with variables, ξ , being electron density or its gradient. With this Fock matrix, we could define a total core Hamiltonian as

$$\mathbf{h} = \mathbf{h}_0 + \vec{\mathbf{M}} \cdot \vec{f}^{\text{ext}} + \mathcal{M}^{\text{ind}} \mathbf{V}, \tag{15}$$

and then, the expression

$$E = \mathbf{P} \cdot \left(\mathbf{h} + \frac{1}{2} \mathbf{I} \mathbf{I} \cdot \mathbf{P} \right) + E_{xc} - \sum_{I} Z_{I} \vec{R}_{I} \cdot \vec{f}^{\text{ext}} - \frac{1}{2} \mathcal{M}^{\text{ind}}$$
$$\cdot \left(\mathcal{F}^{\text{nuc}} - \mathcal{F}^{\text{ele}} + \mathcal{F}^{\text{ext}} \right) + E_{\text{vdW}}^{\text{QM/MM}}$$
(16)

will be used for the calculation of the total energy. The last term is the van der Waals (vdW) interaction between QM and MM regions. Here, we adopt the distance-dependent variance of the classical Lennard-Jones (LJ) 12–6 potential according to Payton *et al.*⁵² The expression is presented in Sec. S1 of the supplementary material.

B. Energy gradient and Hessian matrix

The first derivatives of the energy in Eq. (16) with respective to the QM coordinates, x, can be expressed as

$$E^{x} = \mathbf{P} \cdot \left(\mathbf{h}^{[x]} + \frac{1}{2}\mathbf{I}\mathbf{I}^{[x]} \cdot \mathbf{P}\right) + E_{xc}^{[x]} - \mathbf{W} \cdot \mathbf{S}^{[x]} - \sum_{I} Z_{I} \vec{R}_{I}^{x} \cdot \vec{f}^{\text{ ext}}$$
$$- \mathcal{M}^{\text{ind}} \mathcal{F}^{\text{nuc},[x]} + E_{vdW}^{\text{QM/MM},[x]}, \tag{17}$$

where superscripts with [] refer to the explicit derivatives excluding the contributions from orbital rotations. Here,

$$\mathbf{h}^{[x]} = \mathbf{h}_0^{[x]} + \vec{\mathbf{M}}^{[x]} \cdot \vec{f}^{\text{ ext}} + \mathcal{M}^{\text{ind}} \mathbf{V}^{[x]}, \tag{18}$$

with $V_{\mu\nu}^{[x]} = \langle \phi_{\mu} | \mathcal{F} | \phi_{\nu} \rangle^{[x]}$. The energy weighted density matrix is

$$\mathbf{W} = \frac{1}{2}\mathbf{PFCC}^{\dagger} + \frac{1}{2}\mathbf{CC}^{\dagger}\mathbf{FP} = \mathbf{PFP}.$$
 (19)

The contributions from MM part could be found by differentiating the last two terms in Eq. (10) as

$$E^{\text{MM},x} = -\mathcal{M}^{\text{ind}} \cdot \mathcal{F}^{\text{QM},[x]} + E_{\text{vdW}}^{\text{QM/MM},[x]}, \tag{20}$$

where

$$\mathcal{F}^{\text{QM},[x]} = -\mathbf{V}^{[x]}\mathbf{P} - \mathbf{V}\mathbf{P}^{[x]} + \sum_{I} Z_{I}\mathcal{T}_{I}^{[x]}, \qquad (21)$$

derived from Eq. (6).

The Hessian can then be obtained by directly differentiating the QM gradient in Eq. (17) with respect to the QM coordinates,

$$\begin{split} E^{xy} &= \mathbf{P} \cdot \left(\mathbf{h}^{[xy]} + \frac{1}{2} \mathbf{I} \mathbf{I}^{[xy]} \cdot \mathbf{P} \right) + \mathbf{P}^{y} \cdot \left(\mathbf{h}^{[x]} + \mathbf{I} \mathbf{I}^{[x]} \cdot \mathbf{P} + \mathbf{F}_{xc}^{[x]} \right) \\ &+ E_{xc}^{[xy]} - \mathbf{W} \cdot \mathbf{S}^{[xy]} - \mathbf{W}^{y} \cdot \mathbf{S}^{[x]} - \mathcal{M}^{\text{ind}} \cdot \mathcal{F}^{\text{nuc},[xy]} \\ &- \mathcal{F}^{\text{QM},y} \cdot \mathcal{T}^{-1} \cdot \mathcal{F}^{\text{QM},[x]} + E_{\text{vdW}}^{\text{QM/MM},[xy]}, \end{split} \tag{22}$$

where

$$\mathbf{h}^{[xy]} = \mathbf{h}_0^{[xy]} + \vec{\mathbf{M}}^{[xy]} \vec{f}^{\text{ext}} + \mathcal{M}^{\text{ind}} \cdot \mathbf{V}^{[xy]}, \tag{23}$$

with $V_{\mu\nu}^{[xy]}=\langle\phi_{\mu}|\mathcal{F}|\phi_{\nu}\rangle^{[xy]}$. The MM contributions to the Hessian matrix could be summarized as

$$E^{\text{MM},xy} = -\mathcal{M}^{\text{ind}} \cdot \left(\mathcal{F}^{\text{QM},[xy]} - \mathbf{V}^{[x]} \mathbf{P}^{y} \right) - \mathcal{F}^{\text{QM},y} \cdot \mathcal{T}^{-1} \cdot \mathcal{F}^{\text{QM},[x]} + E_{\cdot,\text{dW}}^{\text{QM}/\text{MM},[xy]}.$$
(24)

Here, \mathbf{P}^{y} includes the derivatives of orbital rotations. The first term represents the MM charges and dipoles induced by the second-order QM potentials and fields with respect to QM nuclear coordinate changes, while the second term is the interaction between first-order QM potentials and fields and MM induced charges and dipoles from another first-order QM potentials and fields perturbed by QM atom displacements.

After the construction of the Hessian matrix in the mass-weighted coordinates, one could obtain the normal modes and corresponding frequencies by diagonalizing the matrix.⁷¹ It is noted that here we do not project out the translations and rotations from the mass-weighted hessian since it only includes the QM–QM block, and it is actually partial Hessian within the QM region. With this treatment, the frequencies of six lowest-frequency modes, which correspond to the translational and rotational degrees of freedom of the pyridine molecule as shown in Fig. S3 of the

supplementary material, are not zero. For the molecule–MNP system, it is rational to ignore the values of QM–MM and MM–MM blocks because of the much larger masses of the elements in MNP than those in the organic molecule, verified by the values shown in Tables S3–S5.

C. Infrared and Raman spectral intensities

IR and Raman spectra provide information about the molecular vibrations. IR spectra can be obtained from light absorption, whereas Raman spectra reflect light scattering process. The IR transitions are governed by the electronic dipole operator $\hat{\mu}$, while the vibrational Raman transitions are controlled by the dipole induced by the oscillating electric field. Only molecular vibrations that cause a change in electric dipole (polarizability) are IR (Raman) active. Therefore, the calculations of IR and Raman *spectral* intensities are closely related to the calculations of nuclear derivatives of electric dipole and polarizability, respectively. ^{66,71,72}

When the perturbation is the external field f_m , the derivatives of total energy in Eq. (10) would give the total dipole moment

$$\mu_m^{\text{tot}} = -\frac{\partial E}{\partial f_m} = \sum_{I} Z_I R_{I,m} - \mathbf{P} \cdot \mathbf{M}_m + \mathcal{M}^{\text{ind}} \cdot \mathcal{R}_m, \tag{25}$$

where the first two terms produce the QM dipole moment as in Eq. (12) and \mathcal{R}_m is the mth column of matrix \mathcal{R} in Eq. (9). For m=0 (the x component), for instance, \mathcal{R}_m is $[R'_{1x}, 1, 0, 0, R'_{2x}, 1, 0, 0, \ldots]$. Then, $\mathcal{M}^{\text{ind}}\mathcal{R}_m$ would be $\sum_j (q_j^{\text{ind}}R'_{jm} + \mu_{j,m}^{\text{ind}})$, with j as the MM atom index.

The first-order changes in the total dipole in Eq. (25) with respect to nuclear displacements could be derived as

$$\mu_m^{\text{tot},x} = \sum_{I} Z_I R_{I,m}^{[x]} - \mathbf{P}^x \cdot \mathbf{M}_m - \mathbf{P} \cdot \mathbf{M}_m^{[x]} + \mathcal{F}^{\text{QM},x} \cdot \mathcal{T}^{-1} \cdot \mathcal{R}_m.$$
 (26)

Here, the last term refers to the monopolar/dipolar response in the MM region. Namely, as one displaces the QM atoms, it leads to a variation in the corresponding potential and field $(\mathcal{F}^{QM,x})$ and thus causes a change to the induced charges and dipoles on MM atoms.

The static electronic polarizability is obtained by differentiating the total dipole moment given by Eq. (25) with respect to the external field $f_{\rm eff}$.

$$\alpha_{mn} = \frac{\partial \mu_m^{\text{tot}}}{\partial f_n} = -\mathbf{P}^n \cdot \mathbf{M}_m + \left(\mathcal{F}^{\text{QM},n} + \mathcal{R}_n \right) \cdot \mathcal{T}^{-1} \cdot \mathcal{R}_m, \tag{27}$$

and its nuclear derivative is derived as

$$\alpha_{mn}^{x} = -\mathbf{P}^{nx} \cdot \mathbf{M}_{m} - \mathbf{P}^{n} \cdot \mathbf{M}_{m}^{[x]} + \mathcal{F}^{QM,nx} \cdot \mathcal{T}^{-1} \cdot \mathcal{R}_{m}$$

$$= -\mathbf{P}^{nx} \cdot \left(\mathbf{M}_{m} + \mathbf{V} \mathcal{T}^{-1} \mathcal{R}_{m}\right) - \mathbf{P}^{n} \cdot \left(\mathbf{M}_{m}^{[x]} + \mathbf{V}^{[x]} \mathcal{T}^{-1} \mathcal{R}_{m}\right)$$

$$= -\mathbf{P}^{nx} \cdot \tilde{\mathbf{M}}_{m} - \mathbf{P}^{n} \cdot \tilde{\mathbf{M}}_{m}^{[x]}, \tag{28}$$

where $\mathcal{F}^{\mathrm{QM},nx} \cdot \mathcal{T}^{-1} \cdot \mathcal{R}_m$ represents the contribution of the MM part, which indicates that the two perturbations *both* act on the QM region (i.e., $\mathcal{F}^{\mathrm{QM},nx}$) in the current framework. It is incorporated into the dipole moment matrix and its derivative matrix in the last line.

The derivatives of density matrix are derived in Appendix A. As in the case of the first-order derivatives of density matrix \mathbf{P}^x or \mathbf{P}^n , only the *first-order derivatives of orbital rotations* are needed in the second-order derivatives of density matrix \mathbf{P}^{nx} , which is known as the 2n+1 rule.^{73,74} The derivatives of orbital rotations are computed by the coupled-perturbed Hartree–Fock (CPHF) equation or *z*-vector equation, which is presented in Appendix B.

To compare with the experimental Raman intensities, one has to compute the dynamic polarizability and its nuclear derivatives. In these calculations, the density response in the QM region and the force–field parameters representing the MM block should both be frequency-dependent. In this work, the derivatives of the density matrix in Eq. (28) are replaced by their frequency-dependent counterpart, which is computed by solving the response equations in Appendix C. Following Refs. 67–69, the static DIM parameters are retained for the metal clusters here.

III. COMPUTATIONAL DETAILS

The QM/DIM method and its analytic energy derivatives are implemented in a locally modified version of the Q-Chem package. The parameters used in this QM/DIM method are listed in Sec. S1 of the supplementary material. Pyridine (Py) molecule and two gold clusters including 18 and 32 gold atoms are chosen as the test system. Based on these components, three complex configurations shown in Fig. 1 are formed: surficial Py-Au₁₈-S, vertical Py-Au₁₈-V, and Py-Au₃₂ with the nearest N-Au distances being 3, 4, and 5 Å. The

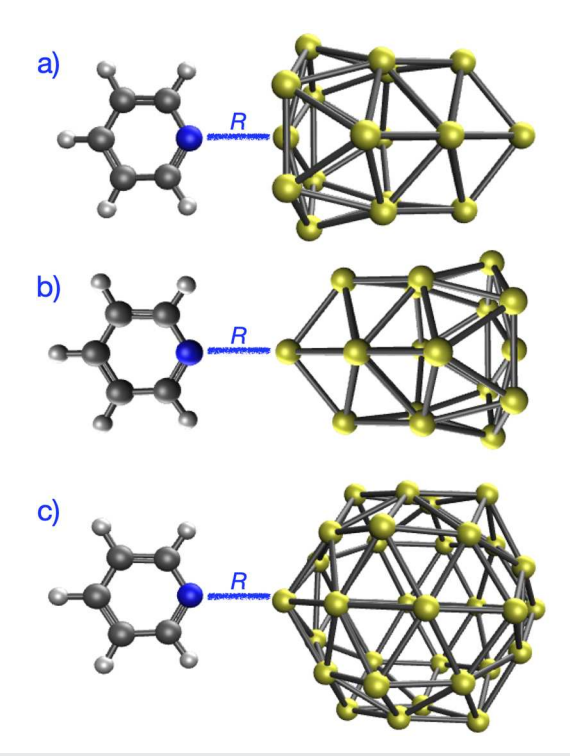


FIG. 1. Pyridine–gold cluster configurations: (a) surfacial Py–Au₁₈–**S**, (b) vertical Py–Au₁₈–**V**, and (c) Py–Au₃₂. The nearest N–Au distance, R, is set to be 3, 4, or 5 Å

geometries are obtained from full QM restrained optimization with a harmonic potential so that each of the structures has only one imaginary frequency along with the labeled N-Au direction; their coordinates are provided in the supplementary material. Restrained optimizations are also carried out by the QM/DIM method, and the obtained coordinates show no apparent difference from full QM results [with largest root mean square deviation (RMSD) value as 0.007 bohr in Table S3 of the supplementary material]. The IR and Raman spectra are calculated by full QM and hybrid QM/DIM methods. In the latter, pyridine is treated by QM and the gold atoms form the DIM region. The partial Hessian is used in the QM/DIM method whose potential errors are discussed in Sec. S3 of the supplementary material. To validate the implementation of the analytic derivatives of the QM/DIM method, analytical and finitedifferent approaches are used to compute the frequencies and Raman spectral intensities of the Py-Au₁₈-V with the labeled N-Au distance as 3 Å, and the values are collected in Table S7 of the supplementary material.

Furthermore, to demonstrate the capability of current analytic derivatives approaches within QM/DIM, we calculate the MNP-mediated Raman spectra of 4,4'-bipyridine (4,4'-BPy), which is set close to the surfaces of Au $_{2057}$ and Ag $_{2057}$ icosahedral MNPs, respectively (their geometric arrangements are shown in Fig. S4 of the supplementary material). An incident field with the wavelength of 532 nm is applied to these systems corresponding to the experimental condition. The simulated spectra are also compared with experimental ones. 76,77

All the calculations are carried out with the PBE0 functional and 6-31+G(d) for N, C, and H atoms and LanL2DZ ECP and basis set for Au atoms using the locally modified Q-Chem 5.2 package.⁷⁵ B3LYP functional is also used for the 4,4′-BPy system for the comparison with previous theoretical works.^{78,79} The convergence thresholds of SCF and CPHF are both 10⁻⁸ a.u. while a 10⁻¹⁴ a.u. threshold is used for two-electron integrals. SG-1 DFT grid⁸⁰ is utilized for DFT numerical integration. The vibrational spectra are plotted using a Lorentz function with a width of 10 cm⁻¹.

IV. RESULTS

A. Infrared spectra

The infrared (IR) spectra of pyridine molecule and three different pyridine–gold complexes (Py–Au $_{18}$ –S, Py–Au $_{18}$ –V, and Py–Au $_{32}$) computed by QM and QM/DIM methods are displayed in Fig. 2. The top row shows the IR spectra of the gas-phase pyridine minimum-energy structure, while the other three rows show the spectra calculated using the optimized configurations (with the distances restrained at 3, 4, and 5 Å). In these three rows, the green curves correspond to the spectra of the pyridine molecule at the geometry extracted from each of these complexes. Overall, the QM/DIM method (blue curves) reproduces similar trends in the harmonic frequency shifts and comparable IR intensities relative to the full QM profiles (red curves) for the tested systems.

Overall, the harmonic vibrational frequencies of the pyridine molecule are shifted by up to 20 cm⁻¹ from the gas phase to the complexes. Within each of the three complexes, however, the frequencies of the adsorbed pyridine molecule have marginal shifts toward higher frequency (smaller than 7 cm⁻¹) upon the binding

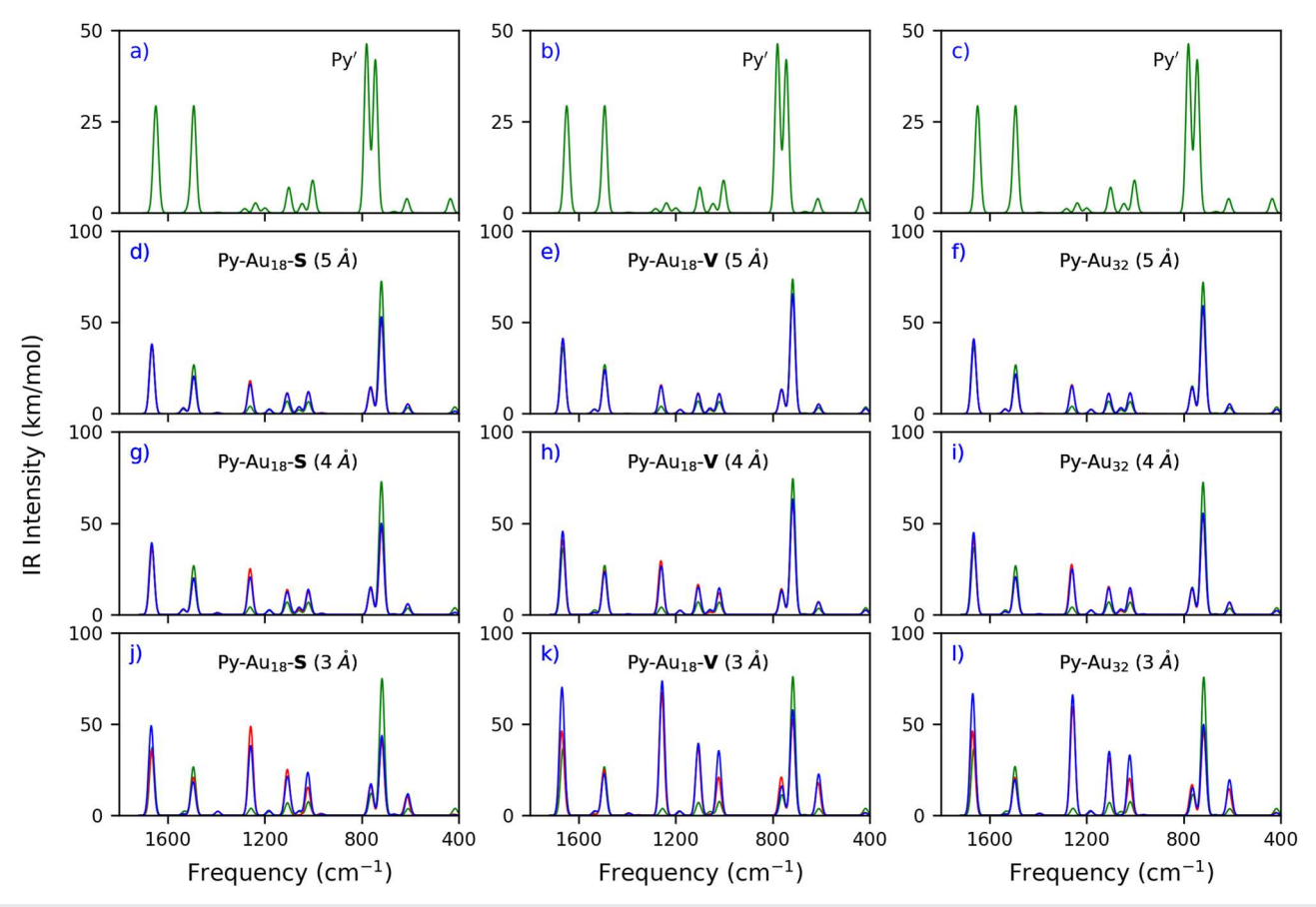


FIG. 2. Infrared spectra of (a)–(c) the gas-phase pyridine (Py') and of (d)–(l) the Py–Au₁₈–**S**, Py–Au₁₈–**V**, and Py–Au₃₂ complexes with three intersystem distances, 3, 4, and 5 Å, calculated by full QM and QM/DIM methods with PBE0/6-31+G(d)/LanL2DZ. The green, red, and blue curves in panels (d)–(l) represent the results from the QM calculation for Py molecules and from full QM and QM/DIM for Py–Au complexes, respectively.

to Au clusters. This is not surprising because the heavy Au atoms vibrate very slowly and have a negligible effect on the nearby pyridine molecule. For a representative structure, Py–Au₁₈–V (3 Å), the numerical values are provided in Table S13 of the supplementary material, and information for several key vibrational modes are collected in Table I.

When the pyridine molecule approaches the Au clusters, the IR peaks of three vibrational modes (ring breathing and two C–H wags) within 1000–1300 cm⁻¹ become increasingly more intense as the distance reduces from 5 to 3 Å. The second C–H wag at 1238 cm⁻¹ is predicted by full QM calculations to have the largest enhancement of 24 times (from 2.7 to 48.7 km/mol) for the S configuration, 33 times for the V configuration, and 24 times for Py–Au₃₂, as shown in the panels (j)–(l) of Fig. 2, respectively. In contrast, some peaks are significantly weakened after the binding to Au clusters. This is especially obvious with the two out-of-plane C–H bends at 744 and 780 cm⁻¹, which have comparable intensities in the gas phase. While only the IR peak at 744 cm⁻¹ is reduced in Py–Au₁₈–S (3 Å) and Py–Au₁₈–V (3 Å) complexes, both peaks (744 and 780 cm⁻¹) lose some strength in the Py–Au₃₂ (3 Å) structure.

These changes in the IR intensities are reproduced reasonably well by QM/DIM calculations, as illustrated in Fig. 2. As shown in Table I, for the Py–Au $_{18}$ –V (3 Å) complex, the aforementioned enhanced C–H wag (mode 16) is predicted to be 67.28 km/mol (full QM) and 73.64 km/mol (QM/DIM). Similarly, the calculated IR intensity of mode 14 is predicted to be enhanced to 35.86 and 38.36 km/mol, respectively, by the full-QM and QM/DIM calculations. The largest deviation appears for mode 22: the full QM method predicts an intensity of 43.62 km/mol, whereas a larger value (66.93 km/mol) is predicted by QM/DIM.

B. Raman scattering spectra

The Raman differential scattering cross section (in unit of cm^2/sr) for the vibrational mode k is calculated as

$$I_k^{\text{Raman}} = \frac{(2\pi)^4}{45} \frac{h}{8\pi^2 c\omega_k} \frac{(\omega_0 - \omega_k)^4}{1 - \exp(-hc\omega_k/k_B T)} S_k(\omega_0)$$
 (29)

based on short-time and Placzek approximations.⁸¹ Here, ω_0 and ω_k are the frequency of the incident light and of kth vibrational mode,

TABLE I. Selected vibrational frequencies and corresponding IR and Raman intensities of gas-phase Py' and Py-Au₁₈-V (3 Å) complexes calculated by full QM and QM/DIM methods with PBE0/6-31+G(d)/LanL2DZ. Here, Py' and Py labels refer to the calculations based on the geometries of Py optimized in gas-phase and in Py-Au₁₈ complexes, respectively.

	Freq. (cm ⁻¹)				I _{IR} (km/mol)				I _{Raman} (Å ⁴ /amu)			
			Py-	-Au ₁₈			P	y-Au ₁₈			Py-Au ₁₈	
No.	Py'	Py	QM	QM/DIM	Py'	Py	QM	QM/DIM	Py'	Py	QM	QM/DIM
3	614.45	609.81	613.18	610.82	3.91	3.65	17.87	22.59	4.48	3.87	8.89	113.51
4	666.96	668.16	666.11	667.73	0.38	0.40	0.04	0.04	5.73	5.04	4.34	6.82
5	744.36	717.01	717.64	717.98	41.94	75.96	52.66	57.79	0.11	0.06	0.30	0.02
6	780.49	761.66	764.78	763.01	46.29	11.29	20.94	16.09	0.04	0.09	0.03	0.03
11	1042.75	1020.11	1025.16	1022.55	0.00	7.58	0.07	35.31	0.01	9.50	0.06	125.08
12	1046.25	1058.45	1057.95	1058.29	2.56	2.05	0.68	0.01	41.41	54.05	294.44	236.31
14	1101.06	1105.89	1108.21	1107.01	7.00	7.00	35.86	38.36	2.17	1.49	2.24	47.73
16	1238.39	1254.27	1257.70	1255.92	2.73	3.72	67.28	73.64	7.58	8.89	9.85	11.21
20	1513.58	1530.22	1534.97	1533.16	1.39	2.15	0.69	2.42	3.67	1.83	8.76	52.45
22	1651.11	1665.77	1670.11	1668.91	22.34	24.82	43.62	66.93	12.86	13.73	12.85	58.09

respectively. S_k (in unit of Å⁴/amu) refers to the Raman scattering (RS) factor,

$$S_k(\omega_0) = 45 \left(\bar{\alpha}^k(\omega_0)\right)^2 + 7 \left(\gamma^k(\omega_0)\right)^2, \tag{30}$$

where isotropic and anisotropic polarizability derivatives, $\tilde{\alpha}^k(\omega_0)$ and $\gamma^k(\omega_0)$, are composed of the components of the changes in molecular dynamic polarizability with respect to the normal mode k as

$$\bar{\alpha}^{k}(\omega_{0}) = \frac{1}{3} \left(\alpha_{xx}^{k}(\omega_{0}) + \alpha_{yy}^{k}(\omega_{0}) + \alpha_{zz}^{k}(\omega_{0}) \right),
\gamma^{k}(\omega_{0}) = \frac{1}{2} \left(\left(\alpha_{xx}^{k}(\omega_{0}) - \alpha_{yy}^{k}(\omega_{0}) \right)^{2} + \left(\alpha_{xx}^{k}(\omega_{0}) - \alpha_{zz}^{k}(\omega_{0}) \right)^{2} \right.
\left. + \left(\alpha_{yy}^{k}(\omega_{0}) - \alpha_{zz}^{k}(\omega_{0}) \right)^{2} + 6 \left(\left(\alpha_{xy}^{k}(\omega_{0}) \right)^{2} + \left(\alpha_{xz}^{k}(\omega_{0}) \right)^{2} \right.
\left. + \left(\alpha_{yz}^{k}(\omega_{0}) \right)^{2} \right),$$
(31)

respectively, where $\alpha_{mn}^k(\omega_0)=\frac{\partial \alpha_{mn}(\omega_0)}{\partial Q_k}$. The normal coordinates, Q, are obtained by transforming the Cartesian coordinates, R, via a transformation matrix L as $Q=L^{-1}R$. L is the eigenvector of the mass-weighted Cartesian Hessian. The constants in Eq. (29) are provided in Table S2.

Figure 3 shows the Raman spectra of Py–Au₁₈–S, Py–Au₁₈–V, and Py–Au₃₂ complexes based on the static electronic polarizability derivatives calculated by full QM and QM/DIM methods. The results are compared to those of the isolated pyridine. For all the configurations, we observe that the Au clusters can significantly enhance the ring breathing vibration mode 12 (around 1050 cm^{$^{-1}$}).

When the distance is 5 Å, although QM/DIM slightly underestimates the intensity of mode 12, it nearly reproduces the full QM spectra as Figs. 3(d)-3(f) show. As R decreases, however, QM/DIM gives less satisfying Raman profiles. Taking the Py-Au₁₈-V system with R=4 Å as an example [see Fig. 3(h)], we observe that QM/DIM

significantly underestimates the intensity of mode 12 but overestimates this of mode 11 compared with the full QM results. When *R* is further shortened to 3 Å, the discrepancy between full QM and QM/DIM results in all frequency ranges increases. As shown in Table I, QM/DIM significantly overestimates the intensities of all the modes except mode 12. In other words, the QM/DIM approach could provide artificial enhancements for some vibrational modes, which can be attributed to the neglect of chemical enhancement and nonlinear responses of the MNP in the current QM/DIM model.

Moreover, we calculate the Raman scattering spectra of 4,4'-bipyridine (4,4'-BPy) in the gas phase and in the proximity of Au_{2057} and Ag_{2057} with respect to the DFT XC functional PBE0 and B3LYP, respectively. The dynamic polarizability derivatives with the incident light of 535 nm are adopted in the calculations. Figures 4 and S5 in the supplementary material show the calculated results, where the gas-phase Raman intensities are scaled by a factor of 20. It is noted that the spectra calculated with PBE0 and B3LYP are almost identical, indicating that the impact of the functional on the spectra is small.

To compare with the experimental off-resonance MNPmediated Raman spectra with the incident light of 535 nm, the differential scattering cross section (in unit of cm²/sr) for the vibrational mode k is calculated based on the dynamic polarizability derivatives. Figure 4 demonstrates that for the adsorbed configurations, QM/DIM predicts a 20 times enhancement for most of the Raman peaks due to electromagnetic enhancement. Both the theoretical calculation and experimental measurement^{76,77} consistent result trend on the MNP-induced changes on the relative spectral intensities. For example, the gold nanoparticle makes the strongest Raman peak of 4,4'-BPy shift to 1678 from 1336 cm⁻¹, the relative intensity at around 1024 cm⁻¹ decreases, and the two Raman peaks in the 600-800 cm⁻¹ range disappear. However, the QM/DIM predictions hardly alter the molecular vibrational frequencies while the experimental frequency shifts could be as large as 18 cm⁻¹.^{76,7} It is unsurprising because after the 4,4'-BPy is adsorbed on the MNP, the QM/DIM optimization yields a similar geometry as the

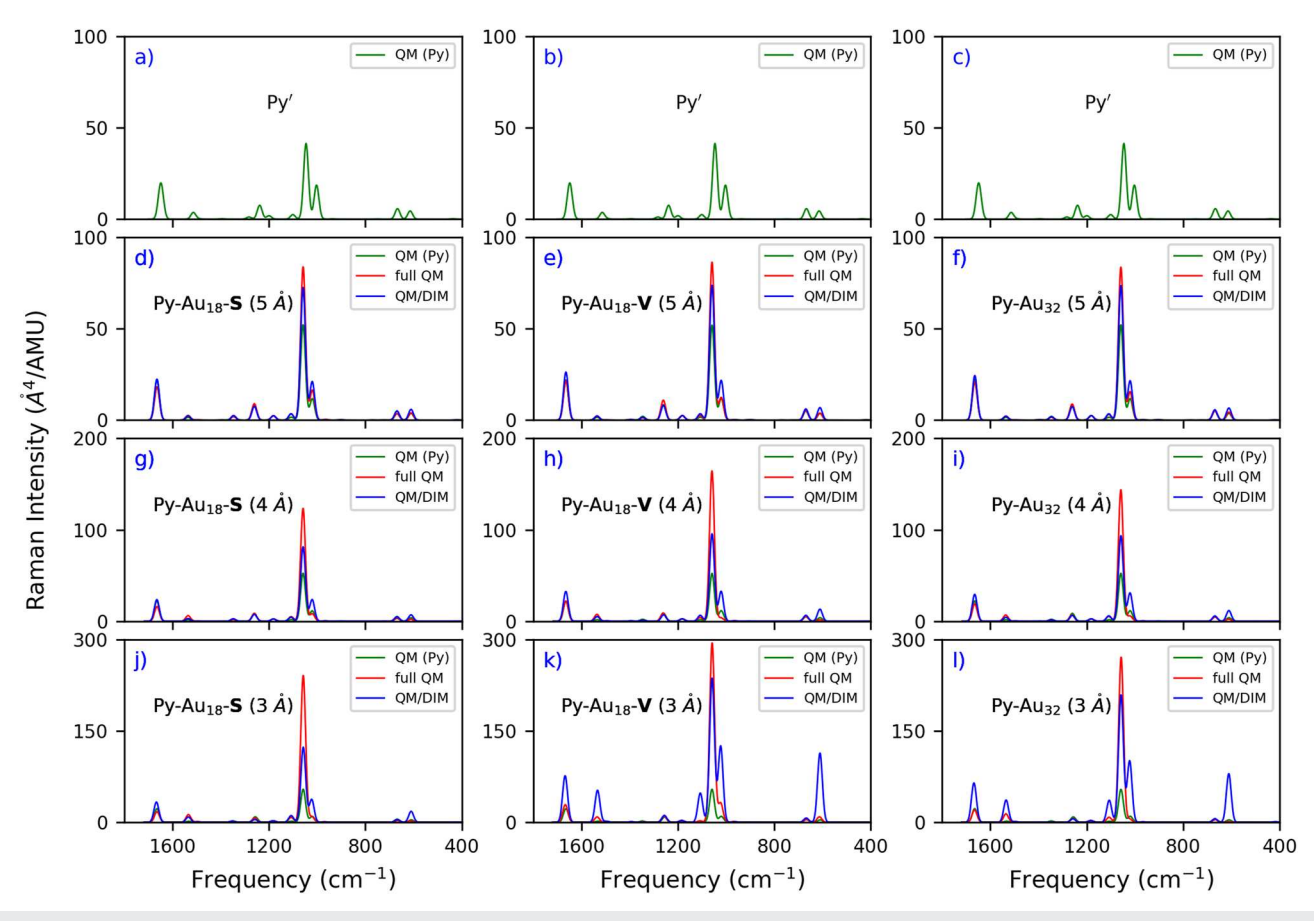


FIG. 3. Raman spectra of (a)–(c) the gas-phase pyridine (Py') and of (d)–(l) the Py–Au₁₈–**V**, and Py–Au₃₂ complexes at 3, 4, and 5 Å intersystem distances calculated by full QM and QM/DIM methods with PBE0/6-31+G(d)/LanL2DZ at $\omega_0=0$.

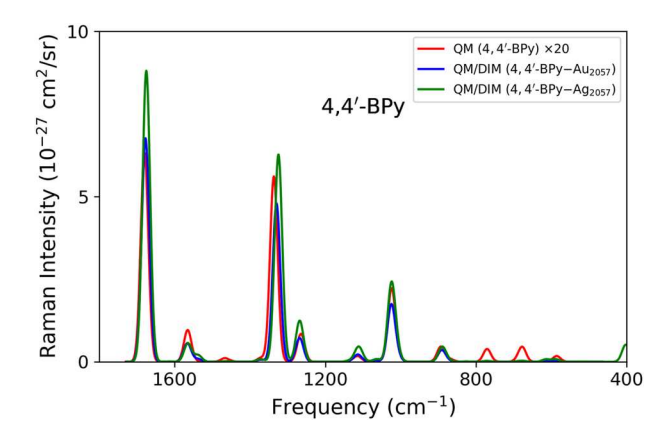


FIG. 4. The Raman spectra of the gas-phase 4,4′-bipyridine (4,4′-BPy), 4,4′-BPy-Au $_{2057}$, and 4,4′-BPy-Ag $_{2057}$ complexes calculated by QM and QM/DIM methods with PBE0/6-31+G(d) under the incident light of 532 nm, where QM peaks are scaled by 20 for comparison. The nearest N–Au and N–Ag bond lengths are 3.034 and 2.996 Å, respectively.

gas-phase one, thus producing only small changes in the vibrational frequencies. This is in line with the Raman spectra of the Py cases. As shown in Table I, the frequencies calculated by full QM and QM/DIM methods have similar values. The large frequency changes after molecule adsorbed on MNP come from geometry differences between Py gas-phase minimum and full QM optimized Py–Au $_{18}$ complexes.

C. Contribution of nonlinear response of MNP to Raman intensity

To shed light on the issue of the QM/DIM approach in the Raman calculations, we calculate the nuclear derivatives of the polarizability through the finite-difference (FD) method based on classical turning points (CTP). Two vibrational modes are chosen: the ring breathing modes around 1020 and 1050 cm⁻¹ (modes 11 and 12). As shown in Fig. 5, the pyridine nitrogen atom shows little participation in the vibrational pattern of mode 12 while it gets involved in that of mode 11 (the same for other artificially enhanced modes).

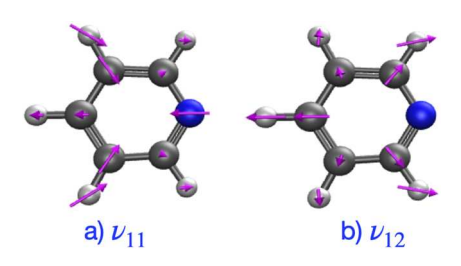


FIG. 5. Vibrational patterns of modes (a) 11 and (b) 12 of pyridine.

As Eq. (27) shows, the molecular electric polarizability α_{mn} is related to the density matrix derivatives with respect to the external field and molecular dipole moment matrix. We can divide the value of α_{mn} into four terms with respect to the atomic basis sets contributed by its two components: the Py molecule and Au cluster. As shown in Table II, for mode 11, the Au cluster contributes 8.877 a.u. to the final polarizability change, which largely cancels the other contributions; while the value (-0.519 a.u.) is negligible for mode 12. This distinction could be understood from the vibrational motions of the pyridine. The nitrogen atom plays a major role in the vibration of the ring breathing mode 11 in Fig. 5(a) and changes the local fields exerted on the Au clusters, which requires the contribution from high-order nonlinear response terms, i.e., the hyperpolarizability-related terms of the Au atoms, to be incorporated. On the other hand, as the vibration of ring stretch mode 12 in Fig. 5(b) is symmetric along the chosen z axis, there is no change in the polarizability of the Au cluster. Furthermore, there is no explicit contribution from the metal atoms to the Raman intensities in the current QM/DIM method, which can be revealed by comparing Eqs. (26) and (28).

As stated for Eq. (28), in the current QM/DIM scheme, the contribution of the MM region only comes from the induced charges and dipoles by the second-order potentials and fields of the QM counterpart, where the induced dipole moments are proportional to the first power of the field intensity. MNP may possess a strong nonlinear response, and the induced dipole moments should include the nonlinear terms that are proportional to the second and higher powers of the field intensity. Therefore, it is reasonable to account for the nonlinear response of MNPs.

The incorporation of the hyperpolarizability has been proposed by Andrews *et al.* in their analysis of molecular Raman scattering mediated by another molecule. 82,83 The corresponding formula in their derivations is 82

$$\alpha_{mn}^{x} = \sum_{kl} R_{AB}^{-3} (\delta_{kl} - 3\hat{e}_{k}\hat{e}_{l}) \mu_{l}^{A,x} \beta_{mnk}^{B},$$
 (32)

where R_{AB} is the inter-distance between two fragments, A and B; \hat{e}_k is a unit number at kth direction; $\vec{\mu}^{A,x}$ is the nuclear derivatives of the ground state dipole moment of A; and β^{B} represents the electric hyperpolarizability tensor of B. It corresponds to the event that the incident and scattered photons of the Raman scattering are on the same fragment A; meanwhile, one virtual photon is exchanged between the two fragments, i.e., excitation energy transfer (EET) occurs between two locally excited states of the two molecules. We note that to arrive at the hyperpolarizability-dipole interaction expression in Eq. (32), two approximations are made for the coupling between the two locally excited states: the exchange integrals are ignored and a multipole expansion of the Coulomb interaction operator is adopted. (The third one is that chargetransfer excitations are not into consideration.) This expression, however, is incomplete because the distance could also be differentiable rather than taking the first-order term in dipole moment [shown in Eq. (37)].

On other hand, if the hyperpolarizability $\beta^{\rm MM}$ is introduced in the QM/DIM at the beginning, the additional term of the energy would be

$$E = \frac{1}{2} \sum_{mnl} \beta_{mnl}^{MM} (f_m^{QM} + f_m^{ext}) (f_n^{QM} + f_n^{ext}) (f_l^{QM} + f_l^{ext})$$
(33)

whose second-order derivative with respect to external field is

$$\alpha_{ij} = \frac{1}{2} \sum_{mnl} \beta_{mnl}^{MM} \left[3f_m^{QM,ij} (f_n^{QM} + f_n^{ext}) (f_l^{QM} + f_l^{ext}) + 6(f_m^{QM,i} + \delta_{im}) (f_n^{QM,j} + \delta_{jn}) (f_l^{QM} + f_l^{ext}) \right].$$
(34)

Then, its nuclear derivative is derived as

$$\alpha_{ij}^{x} = \sum_{mnl} 3\beta_{mnl}^{MM} \left(f_{m}^{QM,i} + \delta_{im} \right) \left(f_{n}^{QM,j} + \delta_{jn} \right) f_{l}^{QM,x}, \tag{35}$$

$$+\sum_{mnl} \beta_{mnl}^{MM} f_l^{QM} \left[6 f_m^{QM,ix} \left(f_n^{QM,j} + \delta_{jn} \right) + 3 f_m^{QM,ij} f_n^{QM,x} + \frac{3}{2} f_m^{QM,ijx} f_n^{QM} \right]. \tag{36}$$

Here, we had assumed $f^{\text{ext}} = 0$ as in the case of no external field. The first line at the right-hand side in the above expression closely

TABLE II. Finite-difference polarizability derivatives (a.u.) for two vibrational modes (1020.11 and 1058.45 cm⁻¹) of Py and Py–Au₁₈–V configurations at 3 Å intermolecular distance calculated by the full QM method with PBE0/6-31+G(d)/LanL2DZ.

		$\mathbf{P}^z \cdot \Delta \mathbf{M}_z$					$\Delta \mathbf{P}^z \cdot \mathbf{M}_z$			
		Py	Py-Au	Au-Py	Au	Py	Py-Au	Au-Py	Au	$\Delta \alpha_{zz}$
11	Gas-phase Full QM	12.556 8.244	-6.455	-6.455	0.000	-9.862 -22.239	6.047	6.047	8.877	2.694 -5.932
12	Gas-phase Full QM	1.419 -5.332	-2.057	-2.057	0.000	-6.481 -32.657	12.617	12.617	-0.519	-5.062 -17.390

TABLE III. Hyperpolarizability (a.u.) of the Au₁₈ cluster calculated using finite-difference with a field strength of 0.001 a.u. at the PBE0/LanL2DZ level. Coordinates are obtained from the restrained optimization of Py–Au₁₈–**V** (3 Å).

		x	y	z
	x	3.979	0.218	-338.778
x	y	0.218	3.168	-20.482
	\overline{z}	-338.778	-20.482	-10.166
	x	0.218	3.168	-20.482
y	y	3.168	0.944	-792.040
•	\overline{z}	-20.482	-792.040	0.337
	x	-338.778	-20.482	-10.166
z	y	-20.482	-792.040	0.337
	z	-10.166	0.337	1929.883

resembles Eq. (32): Provided that the electric field is generated by a dipole as $f_l^{\rm QM} = R_{\rm AB}^{-3} (\delta_{kl} - 3\hat{e}_k \hat{e}_l) \mu_l^{\rm A}$, its nuclear derivative would be

$$f_l^{\,\mathrm{QM},x} = R_{\,\mathrm{AB}}^{\,-3} \big(\delta_{kl} - 3\hat{e}_k \hat{e}_l\big) \mu_l^{\,\mathrm{A},x} + \big(R_{\,\mathrm{AB}}^{\,-3} \big(\delta_{kl} - 3\hat{e}_k \hat{e}_l\big)\big)^x \mu_l^{\,\mathrm{A}}. \tag{37}$$

Then, the interaction of the first term and the hyperpolarizability yields Eq. (32), while the second term is from the derivatives of the distance rather than the molecular dipole. The rest contributions to the nuclear derivatives of polarizability $\alpha_{ij}^{\rm w}$ in Eq. (36) include the expression $\beta_{mnl}^{\rm MM} f_l^{\rm QM}$, referring to the first-order change in metal's polarizability induced by QM field. As in the QM/DIM method, each metal atom is induced by QM potential and field by atomic capacitance and polarizability and the induced charges and dipoles interact with each other, it would be difficult to distinguish this mutual polarization from the contributions in Eq. (36) with the use of molecular hyperpolarizability parameters for metal clusters. Therefore, we use Eq. (35) to account the effect of hyperpolarizability of metal in the following.

This correction is sufficient for our purpose because the gold cluster has large hyperpolarizability, and it has little participation in the vibrational modes of the Raman spectral region we are interested in. The hyperpolarizability of the Au_{18} cluster calculated by the finite-difference method with a field strength of 0.001 a.u. is given in Table III. Consistent values are obtained with a smaller field strength (0.0002 a.u.). As demonstrated in Table III, the calculated hyperpolarizability of the Au_{18} cluster has large components along the z axis, comparable with the values reported in the literature. 84,85

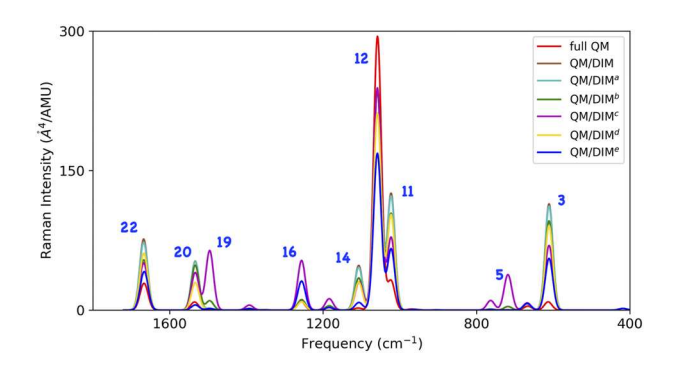


FIG. 6. Corrected Raman spectrum of the Py–Au₁₈–**V** (3 Å) complex by QM/DIM with PBE0/6-31+G(d)/LanL2DZ. (a–c) variations of the QM/DIM method use Eq. (32) with different distance R_{AB} while (d) and (e) correspond to Eq. (35) without and with QM induced fields, respectively.

The corrected QM/DIM Raman intensities of selected modes of the Py-Au₁₈-V (3 Å) complex is shown in Table IV. There are five variations (a-e) of the hyperpolarizability-related correction for the QM/DIM method since some arbitrariness arises when only the molecular hyperpolarizability parameter is available rather than the atomic ones. The (a), (b), and (c) columns are calculated by taking the distance R_{AB} in Eq. (32) as the distance between the two centers of mass (COM), the COM of pyridine and the location of the nearest gold atom, and the shortest distance of the two fragments, respectively. In other words, the distance R_{AB} reduces gradually when moving from (a) to (c). The (d) and (e) columns collect the Raman intensities corrected using Eq. (35) without and with QM induced fields, respectively. Even though the QM/DIM Raman intensity of mode 11 is still larger than the full QM one, it is unsurprisingly reduced with the correction of the hyperpolarizability dependent term. On the other hand, the intensity of mode 12 is also slightly increased by the (a), (b), and (c) corrections.

Figure 6 displays the corrected QM/DIM Raman spectrum of the Py–Au₁₈–V (3 Å) complex. For approach (c), even though more correct intensity is reproduced for mode 11, several modes are wrongly enhanced, such as 5, 16, and 19. It reflects that the distance is very small within this calculation. When the distance is larger, for instance, in the case of approach (b), the green curve moderately approaches the QM one in Fig. 6. On the other hand, the (e) profile (blue line) improves the intensities of almost all the vibrational modes except that the intensity of mode 16 is overestimated and that

TABLE IV. Corrected Raman intensities (Å 4 /amu) by QM/DIM and reference intensities by full QM for vibrational modes 11 and 12 of the Py–Au₁₈–**V** (3 Å) complex with PBE0/6-31+G(d)/LanL2DZ. (a–c) variations of the QM/DIM method use Eq. (32) with different distance R_{AB} while (d) and (e) correspond to Eq. (35) without and with QM induced fields, respectively.

I QM/DIM Raman								
No.	0 a		ь	b c		d e		
11	125.361	122.367	103.807	78.106	102.574	65.860	31.707	
12	236.590	236.679	237.306	238.874	211.852	168.580	294.444	

TABLE V. Charge populations on the pyridine molecule within the different Py-Au complexes calculated from the Mulliken,86 ChEIPG,87 ESP,88 and FBH89 population schemes with PBE0/6-31+G(d)/LanL2DZ.

	$Py-Au_{18}-S$			$Py-Au_{18}-V$			Py-Au ₃₂		
	5 Å	4 Å	3 Å	5 Å	4 Å	3 Å	5 Å	4 Å	3 Å
Mulliken	-0.12	-0.23	-0.01	-0.01	-0.02	0.12	-0.00	-0.00	0.09
ChElPG	-0.06	-0.09	-0.05	-0.03	-0.01	0.09	-0.05	-0.04	0.01
ESP	0.00	-0.00	0.02	0.01	0.04	0.16	-0.00	0.02	0.10
FBH	0.00	0.01	0.05	0.00	0.02	0.10	0.00	0.02	0.08

of mode 12 is further reduced relative to the uncorrected QM/DIM result (from 236 to 168 Å⁴/amu, while the full QM reference is 294 Å⁴/amu). It is acceptable although that these corrections could not produce overall satisfying intensities for all the modes because only the molecular hyperpolarizability of the gold cluster is employed in these calculations rather than the distributed atomic hyperpolarizabilities while the fields and their derivatives act on individual gold atoms.

D. Population analysis

Raman signals can be enhanced by the chemical enhancement and the electromagnetic enhancement. In the current QM/DIM scheme, we do not account for the intermolecular charge transfer (CT) effect, which may be partially responsible for the limited accuracy of the QM/DIM scheme for Raman spectral calculations, especially when the intermolecular distance is short. To check this effect, we calculated the amount of charges on the pyridine molecule within the complexes as shown in Table V.

Among the four used population methods, only the electrostatic potential (ESP) and fragment-based Hirshfeld (FBH) charge schemes consistently predict the expected trend in the fragment charge population, namely, an enhanced CT with a shorter distance between two fragments. These values clearly show that the net transferred charge between Py and Au cluster is almost zero when the nearest distance between these two fragments is 5 Å, while it can be as large as 0.16 e when the distance shortens to 3 Å in Py-Au₁₈-V according to the FBH calculation. It suggests that the ground state charge migration between the Py molecule and Au cluster might also play an important role in the limited accuracy of our current QM/DIM Raman spectral simulations.

V. CONCLUDING REMARKS

In this work, we derived and implemented the QM/DIM method and its high-order energy derivatives for the calculation of noble MNP-mediated molecular vibrational spectra, including IR and Raman scattering. Taking the complexes composed of a pyridine molecule with MNPs consisting of 18 or 32 gold atoms as testing examples, we assessed the accuracy of the current QM/DIM scheme in the calculations of molecular vibrational frequencies and IR/Raman intensities. The QM/DIM method demonstrates the ability to reproduce the molecular vibrational frequencies and IR spectral intensities obtained using the full QM approach. The Raman profiles from QM/DIM calculations behave well for large intermolecular distances such as 5 Å for the tested complexes, while it shows artificial enhancements at shorter molecule-MNP distances for some of the vibrational modes. Nevertheless, with large MNPs such as Au₂₀₅₇ and Ag₂₀₅₇, the relative peak intensity of simulated MNP-mediated Raman spectra of 4,4'-BPy by the QM/DIM method is comparable with the experimental spectral intensity.

The deviation of QM/DIM results from full QM results for small metal clusters, however, can be partially resolved. By incorporating the first-order nonlinear polarizability of Au clusters and the dipole (or electric field) derivatives of the probe molecule, we can capture the non-negligible three-virtual-photon process of Raman scattering within this hybrid method. With this correction, the Raman spectra for the short-distance configurations of the Py-Au clusters calculated using QM/DIM are improved. We thus suggest that the atomic (distributed) hyperpolarizability of metal atoms should be parameterized within the hybrid QM/DIM method to enable it to describe Raman scattering spectra more accurately. Besides, as investigated by Schatz and the co-worker, 90 the other high-order properties such as dipole-quadrupole and dipole-magnetic-dipole polarizabilities may also play a rule in the Raman intensity if the electric field derivatives are comparable with the field strength.

Furthermore, at short intermolecular distances, the overlap of wave functions opens the possibility of a charge migration between Py and the Au cluster. In those cases, the effect of intermolecular CT on the Raman signal should not be neglected, which may otherwise limit the applicability of the current QM/DIM scheme for Raman spectral simulations. It is therefore desirable to develop a scheme to account for the CT effect in the future QM/MM methods. The use of only QM-QM block Hessian matrix in the current work is also a potential source of small errors in the simulated vibrational spectra. In addition, the vdW interaction between the molecule and MNP could affect the optimized molecular structure and then its vibrational frequencies predicted by using the QM/DIM method.

Finally, we note that the plasmon resonance effect of MNPs has not been taken into account in this work. We expect to include the resonance effect by adopting the frequency-dependent parameters for metal atoms in the future publications, which requires solving complex-valued response equations.

SUPPLEMENTARY MATERIAL

See the supplementary material for parameters used in the DIM model and Raman intensity calculation; configurations of 4,4'-bipyridine (4,4'-BPy) and 4,4'-BPy-Au₂₀₅₇ and 4,4'-BPy-Ag₂₀₅₇ complexes; numerical comparison between finite-difference and analytical results of vibrational frequencies and Raman intensities for Py–Au₁₈–V (3 Å) configurations calculated by the QM/DIM method; numerical results of frequencies and IR and Raman intensities of Py–Au cluster, 4,4'-BPy-Au₂₀₅₇, and 4,4'-BPy-Ag₂₀₅₇ complexes; and optimized geometry coordinates of studied Py–Au cluster complexes.

ACKNOWLEDGMENTS

W.L. acknowledges financial support from the National Natural Science Foundation of China (Grant Nos. 21833006 and 22173074). Y.S. is supported by the National Institutes of Health (Grant No. R01GM135392), National Science Foundation (Grant No. CHE-2102071), and the Office of the Vice President of Research and the College of Art and Sciences at the University of Oklahoma (OU).

AUTHOR DECLARATIONS

Conflict of Interest

The authors have no conflicts to disclose.

Author Contributions

Zheng Pei: Methodology (equal); Software (equal); Writing – original draft (equal). Yuezhi Mao: Writing – review & editing (equal). Yihan Shao: Methodology (equal); Software (equal); Writing – review & editing (equal). WanZhen Liang: Methodology (equal); Project administration (equal); Supervision (equal); Writing – review & editing (equal).

DATA AVAILABILITY

The data that support the findings of this study are available within the article and its supplementary material.

APPENDIX A: DERIVATIVES OF DENSITY MATRIX

The occupied MO coefficients could be expanded to the second-order in orbital rotations Θ_{vo} as Ref. 91 suggested,

$$\mathbf{C}_{o} \rightarrow \mathbf{C}_{o} + \mathbf{C}_{v}\Theta_{vo} - \frac{1}{2}\mathbf{C}_{o}\Theta_{vo}^{T}\Theta_{vo}.$$
 (A1)

Its first-order derivative is

$$\mathbf{C}_{o}^{x} \to \mathbf{C}_{o}^{[x]} + \mathbf{C}_{v}^{[x]} \Theta_{vo} + \mathbf{C}_{v} \Theta_{vo}^{[x]} \to \mathbf{C}_{o}^{[x]} + \mathbf{C}_{v} \Theta_{vo}^{[x]}$$
(A2)

without second-order terms while the second-order derivative could be further written as

$$\mathbf{C}_{o}^{xy} \rightarrow \mathbf{C}_{o}^{[xy]} + \mathbf{C}_{v}^{[x]} \Theta_{vo}^{[y]} + \mathbf{C}_{v}^{[y]} \Theta_{vo}^{[x]} + \mathbf{C}_{v} \Theta_{vo}^{[xy]}$$

$$- \frac{1}{2} \left(\mathbf{C}_{o} \Theta_{vo}^{[x],T} \Theta_{vo}^{[y]} + \mathbf{C}_{o} \Theta_{vo}^{[y],T} \Theta_{vo}^{[x]} \right), \tag{A3}$$

where we set $\Theta_{vo} = 0$ as the MOs are optimized. Here,

$$\mathbf{C}_{o}^{[x]} = -\frac{1}{2}\mathbf{C}\mathbf{C}^{T}\mathbf{S}^{[x]}\mathbf{C}_{o}, \qquad \mathbf{C}_{v}^{[x]} = -\frac{1}{2}\mathbf{C}\mathbf{C}^{T}\mathbf{S}^{[x]}\mathbf{C}_{v}.$$
(A4)

When the perturbation (x) in Eq. (A2) is the external field in the n direction, it is simplified to

$$\mathbf{C}_{\mathrm{o}}^{n} = \mathbf{C}_{\mathrm{v}} \boldsymbol{\Theta}_{\mathrm{vo}}^{[n]}. \tag{A5}$$

Similarly, if the second perturbation (y) in Eq. (A3) is the external field in the nth direction, it reduces to

$$\mathbf{C}_{o}^{xn} \to \mathbf{C}_{v}^{[x]} \boldsymbol{\Theta}_{vo}^{[n]} + \mathbf{C}_{v} \boldsymbol{\Theta}_{vo}^{[xn]} - \frac{1}{2} \left(\mathbf{C}_{o} \boldsymbol{\Theta}_{vo}^{[x],T} \boldsymbol{\Theta}_{vo}^{[n]} + \mathbf{C}_{o} \boldsymbol{\Theta}_{vo}^{[n],T} \boldsymbol{\Theta}_{vo}^{[x]} \right). \tag{A6}$$

As the derivatives of density matrix are dependent on the derivatives of occupied MOs,

$$\mathbf{P}^{x} = \mathbf{C}_{o}^{x} \mathbf{C}_{o}^{T} + \mathbf{C}_{o} \mathbf{C}_{o}^{x,T},$$

$$\mathbf{P}^{xy} = \mathbf{C}_{o}^{xy} \mathbf{C}_{o}^{T} + \mathbf{C}_{o} \mathbf{C}_{o}^{xy,T} + \mathbf{C}_{o}^{y} \mathbf{C}_{o}^{x,T} + \mathbf{C}_{o}^{y} \mathbf{C}_{o}^{x,T},$$
(A7)

we have

$$\mathbf{P}^{x} = \mathbf{C}_{o}^{[x]} \mathbf{C}_{o}^{T} + \mathbf{C}_{o} \mathbf{C}_{o}^{[x],T} + \mathbf{C}_{v} \boldsymbol{\Theta}_{vo}^{[x]} \mathbf{C}_{o}^{T} + \mathbf{C}_{o} \boldsymbol{\Theta}_{vo}^{[x],T} \mathbf{C}_{v}^{T}$$

$$= \mathbf{C} \begin{pmatrix} -\mathbf{S}_{oo}^{[x]} & -\frac{1}{2} \mathbf{S}_{ov}^{[x]} + \boldsymbol{\Theta}_{vo}^{[x],T} \\ -\frac{1}{2} \mathbf{S}_{vo}^{[x]} + \boldsymbol{\Theta}_{vo}^{[x]} & 0 \end{pmatrix} \mathbf{C}^{T}, \quad (A8)$$

$$\mathbf{P}^{n} = \mathbf{C} \begin{pmatrix} 0 & \Theta_{\text{vo}}^{[n],T} \\ \Theta_{\text{vo}}^{[n]} & 0 \end{pmatrix} \mathbf{C}^{T}, \tag{A9}$$

and

$$\begin{split} \mathbf{P}^{xn} &= \mathbf{C}_{\mathbf{v}}^{[x]} \boldsymbol{\Theta}_{\mathbf{vo}}^{[n]} \mathbf{C}_{\mathbf{o}}^{T} + \mathbf{C}_{\mathbf{o}} \boldsymbol{\Theta}_{\mathbf{vo}}^{[n],T} \mathbf{C}_{\mathbf{v}}^{[x],T} + \mathbf{C}_{\mathbf{v}} \boldsymbol{\Theta}_{\mathbf{vo}}^{[xn]} \mathbf{C}_{\mathbf{o}}^{T} + \mathbf{C}_{\mathbf{o}} \boldsymbol{\Theta}_{\mathbf{vo}}^{[xn],T} \mathbf{C}_{\mathbf{v}}^{T} \\ &- \mathbf{C}_{\mathbf{o}} \boldsymbol{\Theta}_{\mathbf{vo}}^{[x],T} \boldsymbol{\Theta}_{\mathbf{vo}}^{[n]} \mathbf{C}_{\mathbf{o}}^{T} - \mathbf{C}_{\mathbf{o}} \boldsymbol{\Theta}_{\mathbf{vo}}^{[n],T} \boldsymbol{\Theta}_{\mathbf{vo}}^{[x]} \mathbf{C}_{\mathbf{o}}^{T} + \mathbf{C}_{\mathbf{o}}^{T} \boldsymbol{\Theta}_{\mathbf{vo}}^{[n],T} \mathbf{C}_{\mathbf{v}}^{T} \\ &+ \mathbf{C}_{\mathbf{v}} \boldsymbol{\Theta}_{\mathbf{vo}}^{[n]} \mathbf{C}_{\mathbf{o}}^{[x],T} + \mathbf{C}_{\mathbf{v}} \boldsymbol{\Theta}_{\mathbf{vo}}^{[x]} \boldsymbol{\Theta}_{\mathbf{vo}}^{[n],T} \mathbf{C}_{\mathbf{v}}^{T} + \mathbf{C}_{\mathbf{v}} \boldsymbol{\Theta}_{\mathbf{vo}}^{[n]} \boldsymbol{\Theta}_{\mathbf{vo}}^{[x],T} \mathbf{C}_{\mathbf{v}}^{T} \\ &= -\frac{1}{2} \left(\mathbf{C} \mathbf{C}^{T} \mathbf{S}^{[x]} \mathbf{P}^{n} + \mathbf{P}^{n} \mathbf{S}^{[x]} \mathbf{C} \mathbf{C}^{T} \right) \\ &+ \mathbf{C} \begin{pmatrix} -\mathbf{\Theta}_{\mathbf{vo}}^{[x],T} \boldsymbol{\Theta}_{\mathbf{vo}}^{[n]} - \mathbf{\Theta}_{\mathbf{vo}}^{[n],T} \mathbf{\Theta}_{\mathbf{vo}}^{[x]} & \mathbf{\Theta}_{\mathbf{vo}}^{[n],T} + \mathbf{\Theta}_{\mathbf{vo}}^{[n]} \mathbf{\Theta}_{\mathbf{vo}}^{[x],T} \\ \mathbf{\Theta}_{\mathbf{vo}}^{[nx]} & \mathbf{\Theta}_{\mathbf{vo}}^{[x],T} + \mathbf{\Theta}_{\mathbf{vo}}^{[n]} \mathbf{\Theta}_{\mathbf{vo}}^{[x],T} + \mathbf{\Theta}_{\mathbf{vo}}^{[n]} \mathbf{\Theta}_{\mathbf{vo}}^{[x],T} \end{pmatrix} \mathbf{C}^{T}. \end{split}$$
(A10)

The derivatives of orbital rotations $(\Theta_{vo}^{[x]}, \Theta_{vo}^{[n]}, \text{ and } \Theta_{vo}^{[nx]})$ are determined using the procedure outlined in Appendix B.

APPENDIX B: COUPLED-PERTURBED SELF-CONSISTENT FIELD AND z-VECTOR EQUATIONS

To obtain the first-order changes in the density matrix, we need to solve the coupled-perturbed self-consistent field (CPSCF) equation. Differentiating the SCF convergence condition $[\mathbf{F}, \mathbf{P}]_S = \mathbf{FPS} - \mathbf{SPF} = 0$ with respective to an external perturbation x, we have

$$\left[\mathbf{F}^{x},\mathbf{P}\right]_{S}+\left[\mathbf{F},\mathbf{P}^{x}\right]_{S}+\left[\mathbf{F},\mathbf{P}\right]_{S^{x}}=0,\tag{B1}$$

where $\mathbf{F}^x = \mathbf{F}^{[x]} + \mathbf{F}^{(2)} \cdot \mathbf{P}^x$. After moving the \mathbf{P}^x dependent terms to one side, we arrive at

$$\left[\mathbf{F}, \mathbf{P}^{x}\right]_{S} + \left[\mathbf{F}^{(2)} \cdot \mathbf{P}^{x}, \mathbf{P}\right]_{c} = -\left[\mathbf{F}^{[x]}, \mathbf{P}\right]_{c} - \left[\mathbf{F}, \mathbf{P}\right]_{S^{x}}, \tag{B2}$$

where $\mathbf{F}^{(2)} = \mathbf{II} + \mathbf{\Omega} + \mathbf{V} \mathcal{F}^{-1} \mathbf{V}$. Note that $\mathbf{\Omega}$ is the exchange-correlation portion of the response kernel as defined in Eq. (14) of Ref. 70. The explicit Fock matrix derivatives, $\mathbf{F}^{[x]} = \mathbf{h}^{[x]} + \mathbf{II}^{[x]} \cdot \mathbf{P} + \mathbf{F}^{[x]}_{xc}$, where $\mathbf{h}^{[x]}$ includes the contribution from the MM region as shown in Eq. (17) and $\mathbf{F}^{[x]}_{xc}$ is defined in Eq. (25) in Ref. 70. Projecting the first-order equation-of-motion in Eq. (B2) into the vo block, we have

$$(\mathbf{A} + \mathbf{B})\Theta_{\text{vo}}^{[x]} = \mathbf{L}_{\text{vo}}^{[x]}, \tag{B3}$$

where (A+B) is the orbital Hessian, including the Fock derivatives with respect to orbital rotations. The right-hand side is the vo block of the Lagrangian

$$\mathbf{L}^{[x]} = \mathbf{h}_{0}^{[x]} + \mathbf{H}^{[x]} \cdot \mathbf{P} + \mathbf{F}_{xc}^{[x]} + \vec{\mathbf{M}}^{[x]} \vec{f}^{\text{ext}} + (\mathbf{H} + \mathbf{\Omega}) \cdot \mathbf{P}^{[x]}$$
$$- \frac{1}{2} \left(\mathbf{S}^{[x]} \mathbf{C} \mathbf{C}^{T} \mathbf{F} + \mathbf{F} \mathbf{C} \mathbf{C}^{T} \mathbf{S}^{[x]} \right) + \mathcal{M}^{\text{ind}} \mathbf{V}^{[x]} + \mathcal{F}^{\text{tot,}[x]} \mathcal{T}^{-1} \mathbf{V}$$
(B4)

for QM nuclear perturbations, where the last line at the right-hand side represents the contribution from the MM part. In addition, one

$$\mathbf{L}^{[n]} = \mathbf{M}_n + \mathcal{R}_n \mathcal{T}^{-1} \mathbf{V} \tag{B5}$$

to solve for $\Theta_{vo}^{[n]}$ with static external field perturbations. (The dynamic counterpart is concerned in the Appendix C.) The products of property vectors and response properties are interchangeable, for instance, $\Theta_{vo}^{[x]} \cdot \mathbf{L}_{vo}^{[a]} = \mathbf{L}_{vo}^{[x]} \cdot (\mathbf{A} + \mathbf{B})^{-1} \cdot \mathbf{L}_{vo}^{[a]} = \mathbf{L}_{vo}^{[x]} \cdot \Theta_{vo}^{[a]}$.

The second-order CPSCF equation derived from Eq. (B1) is

$$\begin{aligned} \left[\mathbf{F}^{nx}, \mathbf{P}\right]_{\mathbf{S}} + \left[\mathbf{F}^{n}, \mathbf{P}^{x}\right]_{\mathbf{S}} + \left[\mathbf{F}^{x}, \mathbf{P}^{n}\right]_{\mathbf{S}} + \left[\mathbf{F}, \mathbf{P}^{nx}\right]_{\mathbf{S}} \\ + \left[\mathbf{F}^{n}, \mathbf{P}\right]_{\mathbf{S}^{x}} + \left[\mathbf{F}, \mathbf{P}^{n}\right]_{\mathbf{S}^{x}} = 0, \end{aligned} \tag{B6}$$

with hybrid nuclear coordinate (x) and external field (n) perturbations. Here,

$$\mathbf{F}^{n} = \mathbf{M}_{n} + \mathcal{R}_{n} \mathcal{T}^{-1} \mathbf{V} + (\mathbf{II} + \mathbf{\Omega}) \cdot \mathbf{P}^{n},$$

$$\mathbf{F}^{nx} = \mathbf{M}_{n}^{[x]} + \mathcal{R}_{n} \mathcal{T}^{-1} \mathbf{V}^{[x]} + (\mathbf{II}^{[x]} + \mathbf{\Omega}^{[x]}) \cdot \mathbf{P}^{n} + (\mathbf{II} + \mathbf{\Omega}) \cdot \mathbf{P}^{nx}$$
(B7)

After moving P^{nx} -dependent terms to one side of Eq. (B6) and keeping only the vo block, we arrive at

$$(\mathbf{A} + \mathbf{B})\Theta_{\text{vo}}^{[nx]} = \mathbf{L}_{\text{vo}}^{[nx]}, \tag{B8}$$

with

$$\mathbf{L}^{[nx]} = -\left[\mathbf{F}, \mathbf{P}^{n}\right]_{\mathbf{S}^{x}} - \left[\mathbf{F}^{n}, \mathbf{P}\right]_{\mathbf{S}^{x}} - \left[\mathbf{F}^{[nx]}, \mathbf{P}\right]_{\mathbf{S}} - \left[\mathbf{F}, \mathbf{P}^{[nx]}\right]_{\mathbf{S}}$$
$$-\left[\mathbf{F}^{n}, \mathbf{P}^{x}\right]_{\mathbf{S}} - \left[\mathbf{F}^{x}, \mathbf{P}^{n}\right]_{\mathbf{S}}.$$
 (B9)

Instead of explicitly solving the second-order response in Eq. (B8), however, we can directly compute the desired product $\mathbf{P}_{vo}^{xn} \cdot \tilde{\mathbf{M}}_{m,vo}$ in Eq. (28) as

$$\Theta_{\text{vo}}^{[nx]} \cdot \left(\tilde{\mathbf{M}}_{m}\right)_{\text{vo}} = \left(\mathbf{L}_{\text{vo}}^{[nx]} \cdot \left(\mathbf{A} + \mathbf{B}\right)^{-1}\right) \cdot \left(\tilde{\mathbf{M}}_{m}\right)_{\text{vo}} = \mathbf{L}_{\text{vo}}^{[nx]} \cdot \Theta_{\text{vo}}^{[m]}$$
(B10)

by interchanging the variables. It corresponds to the well-known 2n+1 rule. 92

APPENDIX C: FREQUENCY-DEPENDENT RESPONSES

When an external frequency-dependent field is applied, one needs to go beyond Eq. (B3) and adopt a non-Hermitian formula, 93

$$\begin{bmatrix} \begin{pmatrix} \mathbf{A} & \mathbf{B} \\ \mathbf{B} & \mathbf{A} \end{pmatrix} - \omega \begin{pmatrix} \mathbf{1} & \mathbf{0} \\ \mathbf{0} & -\mathbf{1} \end{pmatrix} \end{bmatrix} \begin{pmatrix} X^n \\ Y^n \end{pmatrix} = \begin{pmatrix} \mathbf{L}_{vo}^{[n]} \\ \mathbf{L}_{vo}^{[n],*} \end{pmatrix}, \tag{C1}$$

where ω is the frequency of the applied field and $\mathbf{L}_{vo}^{[n]}$ at the right-hand side is the dipole moment defined in Eq. (B5). This equation could be written as

$$(\Lambda - \omega \Delta)|X^n; Y^n\rangle = -|L_{vo}^{[n]}; L_{vo}^{[n]}\rangle$$
 (C2)

for simplicity, with

$$\Lambda = \begin{pmatrix} \mathbf{A} & \mathbf{B} \\ \mathbf{B} & \mathbf{A} \end{pmatrix}, \qquad \Delta = \begin{pmatrix} \mathbf{1} & \mathbf{0} \\ \mathbf{0} & -\mathbf{1} \end{pmatrix}. \tag{C3}$$

After the response equation is solved for all the *x*, *y*, and *z* directions, the corresponding first-order density matrix is formed as

$$\mathbf{P}^{n}(\omega) = \mathbf{C} \begin{pmatrix} 0 & \mathbf{Y}^{n,\dagger} \\ \mathbf{X}^{n} & 0 \end{pmatrix} \mathbf{C}^{\dagger}.$$
 (C4)

Then, the nuclear derivatives of amplitude responses in Eq. (C2) follow

$$(\Lambda - \omega \Delta)|X^n; Y^n\rangle^x = -(\Lambda - \omega \Delta)^x |X^n; Y^n\rangle - \left|L_{vo}^{[n]}; L_{vo}^{[n]}\right|^x = L^{nx},$$
(C5)

which closely resembles Eq. (B8) and can be solved using the same iterative procedure for handling the coupled-perturbed equation in Eq. (B8) but with the matrix dimension doubled.

REFERENCES

¹S. Eustis and M. A. El-Sayed, "Why gold nanoparticles are more precious than pretty gold: Noble metal surface plasmon resonance and its enhancement of the radiative and nonradiative properties of nanocrystals of different shapes," Chem. Soc. Rev. 35, 209–217 (2006).

²S. A. Maier, Plasmonics: Fundamentals and Applications (Springer, New York, 2007).

³M. Pelton and G. W. Bryant, *Introduction to Metal-Nanoparticle Plasmonics* (Wiley: Science Wise Publishing, Hoboken, NJ, 2013).

⁴J. Langer, D. Jimenez de Aberasturi, J. Aizpurua, R. A. Alvarez-Puebla, B. Auguié, J. J. Baumberg, G. C. Bazan, S. E. J. Bell, A. Boisen, A. G. Brolo, J. Choo, D. Cialla-May, V. Deckert, L. Fabris, K. Faulds, F. J. García de Abajo, R. Goodacre, D. Graham, A. J. Haes, C. L. Haynes, C. Huck, T. Itoh, M. Käll, J. Kneipp, N. A. Kotov, H. Kuang, E. C. Le Ru, H. K. Lee, J.-F. Li, X. Y. Ling, S. A. Maier, T. Mayerhöfer, M. Moskovits, K. Murakoshi, J.-M. Nam, S. Nie, Y. Ozaki, I. Pastoriza-Santos, J. Perez-Juste, J. Popp, A. Pucci, S. Reich, B. Ren, G. C. Schatz, T. Shegai, S. Schlücker, L.-L. Tay, K. G. Thomas, Z.-Q. Tian, R. P. Van Duyne, T. Vo-Dinh, Y. Wang, K. A. Willets, C. Xu, H. Xu, Y. Xu, Y. S. Yamamoto, B. Zhao, and L. M. Liz-Marzán, "Present and future of surface-enhanced Raman scattering," ACS Nano 14, 28–117 (2019).

⁵W. Hou, W. H. Hung, P. Pavaskar, A. Goeppert, M. Aykol, and S. B. Cronin, "Photocatalytic conversion of CO₂ to hydrocarbon fuels via plasmon-enhanced absorption and metallic interband transitions," ACS Catal. 1, 929–936 (2011).

- ⁶C. Novo, A. M. Funston, and P. Mulvaney, "Direct observation of chemical reactions on single gold nanocrystals using surface plasmon spectroscopy," Nat. Nanotechnol. 3, 598–602 (2008).
- ⁷R. F. Aroca, "Plasmon enhanced spectroscopy," Phys. Chem. Chem. Phys. 15, 5355 (2013).
- ⁸C. D. Geddes, "Metal-enhanced fluorescence," Phys. Chem. Chem. Phys. 15, 19537 (2013).
- ⁹J. Dong, Z. Zhang, H. Zheng, and M. Sun, "Recent progress on plasmonenhanced fluorescence," Nanophotonics 4, 472–490 (2015).
- ¹⁰J.-F. Li, C.-Y. Li, and R. F. Aroca, "Plasmon-enhanced fluorescence spectroscopy," Chem. Soc. Rev. 46, 3962–3979 (2017).
- ¹¹ M. J. Kale, T. Avanesian, H. Xin, J. Yan, and P. Christopher, "Controlling catalytic selectivity on metal nanoparticles by direct photoexcitation of adsorbate–metal bonds," Nano Lett. 14, 5405–5412 (2014).
- ¹²S. Linic, U. Aslam, C. Boerigter, and M. Morabito, "Photochemical transformations on plasmonic metal nanoparticles," Nat. Mater. 14, 567–576 (2015).
- ¹³U. Aslam, V. G. Rao, S. Chavez, and S. Linic, "Catalytic conversion of solar to chemical energy on plasmonic metal nanostructures," Nat. Catal. 1, 656–665 (2018).
- ¹⁴E. Kazuma and Y. Kim, "Mechanistic studies of plasmon chemistry on metal catalysts," Angew. Chem., Int. Ed. 58, 4800–4808 (2019).
- ¹⁵N. Valley, N. Greeneltch, R. P. Van Duyne, and G. C. Schatz, "A look at the origin and magnitude of the chemical contribution to the enhancement mechanism of surface-enhanced Raman spectroscopy (SERS): Theory and experiment," J. Phys. Chem. Lett. 4, 2599–2604 (2013).
- ¹⁶C. Boerigter, R. Campana, M. Morabito, and S. Linic, "Evidence and implications of direct charge excitation as the dominant mechanism in plasmon-mediated photocatalysis," Nat. Commun. 7, 10545 (2016).
 ¹⁷Y. Yu, V. Sundaresan, and K. A. Willets, "Hot carriers versus thermal effects:
- ¹⁷Y. Yu, V. Sundaresan, and K. A. Willets, "Hot carriers versus thermal effects: Resolving the enhancement mechanisms for plasmon-mediated photoelectrochemical reactions," J. Phys. Chem. C 122, 5040–5048 (2018).
- ¹⁸ V. Faessler, C. Hrelescu, A. A. Lutich, L. Osinkina, S. Mayilo, F. Jäckel, and J. Feldmann, "Accelerating fluorescence resonance energy transfer with plasmonic nanoresonators," Chem. Phys. Lett. **508**, 67–70 (2011).
- ¹⁹P. Ghenuche, J. de Torres, S. B. Moparthi, V. Grigoriev, and J. Wenger, "Nanophotonic enhancement of the Förster resonance energy-transfer rate with single nanoapertures," Nano Lett. 14, 4707–4714 (2014).
- ²⁰L.-Y. Hsu, W. Ding, and G. C. Schatz, "Plasmon-coupled resonance energy transfer," J. Phys. Chem. Lett. 8, 2357–2367 (2017).
- ²¹ W. Ding, L.-Y. Hsu, C. W. Heaps, and G. C. Schatz, "Plasmon-coupled resonance energy transfer II: Exploring the peaks and dips in the electromagnetic coupling factor," J. Phys. Chem. C 122, 22650–22659 (2018).
- ²²J. Zhao, A. O. Pinchuk, J. M. McMahon, S. Li, L. K. Ausman, A. L. Atkinson, and G. C. Schatz, "Methods for describing the electromagnetic properties of silver and gold nanoparticles," Acc. Chem. Res. 41, 1710–1720 (2008).
- ²³ L. Jensen, C. M. Aikens, and G. C. Schatz, "Electronic structure methods for studying surface-enhanced Raman scattering," Chem. Soc. Rev. 37, 1061 (2008).
- ²⁴S. M. Morton, D. W. Silverstein, and L. Jensen, "Theoretical studies of plasmonics using electronic structure methods," Chem. Rev. 111, 3962–3994 (2011).
- ²⁵C. M. Aikens and G. C. Schatz, "TDDFT studies of absorption and SERS spectra of pyridine interacting with Au₂₀," J. Phys. Chem. A 110, 13317–13324 (2006).
- ²⁶ J. C. Idrobo, W. Walkosz, S. F. Yip, S. Öğüt, J. Wang, and J. Jellinek, "Static polarizabilities and optical absorption spectra of gold clusters (Au_n , n = 2-14 and 20) from first principles," Phys. Rev. B **76**, 205422 (2007).
- ²⁷S. M. Morton and L. Jensen, "Understanding the molecule-surface chemical coupling in SERS," J. Am. Chem. Soc. 131, 4090–4098 (2009).
- ²⁸ L. Liu, D. Chen, H. Ma, and W. Liang, "Spectral characteristics of chemical enhancement on SERS of benzene-like derivatives: Franck-Condon and Herzberg-Teller contributions," J. Phys. Chem. C 119, 27609–27619 (2015).
- ²⁹ M. J. Trujillo, S. L. Strausser, J. C. Becca, J. F. DeJesus, L. Jensen, D. M. Jenkins, and J. P. Camden, "Using SERS to understand the binding of *N*-heterocyclic carbenes to gold surfaces," J. Phys. Chem. Lett. **9**, 6779–6785 (2018).
- ³⁰R. Chen and L. Jensen, "Interpreting the chemical mechanism in SERS using a Raman bond model," J. Chem. Phys. **152**, 024126 (2020).

- ³¹R. Chen and L. Jensen, "Quantifying the enhancement mechanisms of surfaceenhanced Raman scattering using a Raman bond model," J. Chem. Phys. 153, 224704 (2020).
- ³²X.-G. Zhang, L. Zhang, S. Feng, H. Qin, D.-Y. Wu, and Y. Zhao, "Light driven mechanism of carbon dioxide reduction reaction to carbon monoxide on gold nanoparticles: A theoretical prediction," J. Phys. Chem. Lett. **12**, 1125–1130 (2021).
- ³³J. Mullin, N. Valley, M. G. Blaber, and G. C. Schatz, "Combined quantum mechanics (TDDFT) and classical electrodynamics (Mie theory) methods for calculating surface enhanced Raman and hyper-Raman spectra," J. Phys. Chem. A 116, 9574–9581 (2012).
- ³⁴W. H. Yang, G. C. Schatz, and R. P. Van Duyne, "Discrete dipole approximation for calculating extinction and Raman intensities for small particles with arbitrary shapes," J. Chem. Phys. **103**, 869–875 (1995).
- ³⁵S. Vukovic, S. Corni, and B. Mennucci, "Fluorescence enhancement of chromophores close to metal nanoparticles. Optimal setup revealed by the polarizable continuum model," J. Phys. Chem. C 113, 121–133 (2008).
- ³⁶Á. Sánchez-González, S. Corni, and B. Mennucci, "Surface-enhanced fluorescence within a metal nanoparticle array: The role of solvent and plasmon couplings," J. Phys. Chem. C **115**, 5450–5460 (2011).
- ³⁷O. Andreussi, S. Caprasecca, L. Cupellini, I. Guarnetti-Prandi, C. A. Guido, S. Jurinovich, L. Viani, and B. Mennucci, "Plasmon enhanced light harvesting: Multiscale modeling of the FMO protein coupled with gold nanoparticles," J. Phys. Chem. A 119, 5197–5206 (2014).
- ³⁸J. Applequist, "An atom dipole interaction model for molecular optical properties," Acc. Chem. Res. **10**, 79–85 (1977).
- ³⁹L. Jensen, P.-O. Åstrand, A. Osted, J. Kongsted, and K. V. Mikkelsen, "Polarizability of molecular clusters as calculated by a dipole interaction model," J. Chem. Phys. **116**, 4001–4010 (2002).
- ⁴⁰H. S. Smalø, P.-O. Åstrand, and A. Mayer, "Combined nonmetallic electronegativity equalisation and point-dipole interaction model for the frequency-dependent polarisability," Mol. Phys. 111, 1470–1481 (2013).
- ⁴¹N. Davari, S. Haghdani, P.-O. Åstrand, and G. C. Schatz, "Local electric field factors by a combined charge-transfer and point-dipole interaction model," RSC Adv. 5, 31594–31605 (2015).
- ⁴²A. Mayer, "Formulation in terms of normalized propagators of a charge-dipole model enabling the calculation of the polarization properties of fullerenes and carbon nanotubes," Phys. Rev. B **75**, 045407 (2007).
- ⁴³ A. Mayer, A. L. González, C. M. Aikens, and G. C. Schatz, "A charge-dipole interaction model for the frequency-dependent polarizability of silver clusters," Nanotechnology 20, 195204 (2009).
- ⁴⁴L. L. Jensen and L. Jensen, "Electrostatic interaction model for the calculation of the polarizability of large noble metal nanoclusters," J. Phys. Chem. C 112, 15697–15703 (2008).
- ⁴⁵L. L. Jensen and L. Jensen, "Atomistic electrodynamics model for optical properties of silver nanoclusters," J. Phys. Chem. C 113, 15182–15190 (2009).
- ⁴⁶X. Chen, J. E. Moore, M. Zekarias, and L. Jensen, "Atomistic electrodynamics simulations of bare and ligand-coated nanoparticles in the quantum size regime," Nat. Commun. 6, 8921 (2015).
- ⁴⁷J. Lim, S. Kang, J. Kim, W. Y. Kim, and S. Ryu, "Non-empirical atomistic dipole-interaction-model for quantum plasmon simulation of nanoparticles," Sci. Rep. 7, 15775 (2017).
- ⁴⁸S. T. Olsen and K. V. Mikkelsen, "First hyperpolarizability of *para*-aminoaniline induced by a variety of gold nano particles," Phys. Chem. Chem. Phys. **18**, 24343–24349 (2016).
- ⁴⁹I. M. I. Boye, M. H. Hansen, and K. V. Mikkelsen, "The influence of nanoparticles on the polarizabilities and hyperpolarizabilities of photochromic molecules," Phys. Chem. Chem. Phys. **20**, 23320–23327 (2018).
- ⁵⁰S. M. Morton and L. Jensen, "A discrete interaction model/quantum mechanical method for describing response properties of molecules adsorbed on metal nanoparticles," J. Chem. Phys. 133, 074103 (2010).
- ⁵¹S. M. Morton and L. Jensen, "A discrete interaction model/quantum mechanical method to describe the interaction of metal nanoparticles and molecular absorption," J. Chem. Phys. 135, 134103 (2011).

- ⁵²J. L. Payton, S. M. Morton, J. E. Moore, and L. Jensen, "A discrete interaction model/quantum mechanical method for simulating surface-enhanced Raman spectroscopy," J. Chem. Phys. 136, 214103 (2012).
- ⁵³J. M. Rinaldi, S. M. Morton, and L. Jensen, "A discrete interaction model/quantum mechanical method for simulating nonlinear optical properties of molecules near metal surfaces," Mol. Phys. 111, 1322–1331 (2013).
- ⁵⁴Z. Rinkevicius, X. Li, J. A. R. Sandberg, K. V. Mikkelsen, and H. Ågren, "A hybrid density functional theory/molecular mechanics approach for linear response properties in heterogeneous environments," J. Chem. Theory Comput. 10, 989–1003 (2014).
- ⁵⁵A. Fihey, F. Maurel, and A. Perrier, "Plasmon–excitation coupling for dithienylethene/gold nanoparticle hybrid systems: A theoretical study," J. Phys. Chem. C 119, 9995–10006 (2015).
- ⁵⁶Z. Hu and L. Jensen, "A discrete interaction model/quantum mechanical method for simulating plasmon-enhanced two-photon absorption," J. Chem. Theory Comput. 14, 5896–5903 (2018).
- ⁵⁷J. L. Payton, S. M. Morton, J. E. Moore, and L. Jensen, "A hybrid atomistic electrodynamics-quantum mechanical approach for simulating surface-enhanced Raman scattering," Acc. Chem. Res. 47, 88–99 (2014).
- ⁵⁸Z. Hu, D. V. Chulhai, and L. Jensen, "Simulating surface-enhanced hyper-Raman scattering using atomistic electrodynamics-quantum mechanical models," J. Chem. Theory Comput. 12, 5968–5978 (2016).
- ⁵⁹J. C. Becca, X. Chen, and L. Jensen, "A discrete interaction model/quantum mechanical method for simulating surface-enhanced Raman spectroscopy in solution," J. Chem. Phys. 154, 224705 (2021).
- ⁶⁰N. Chiang, N. Jiang, D. V. Chulhai, E. A. Pozzi, M. C. Hersam, L. Jensen, T. Seideman, and R. P. Van Duyne, "Molecular-resolution interrogation of a porphyrin monolayer by ultrahigh vacuum tip-enhanced Raman and fluorescence spectroscopy," Nano Lett. 15, 4114–4120 (2015).
 ⁶¹T. Giovannini, A. Puglisi, M. Ambrosetti, and C. Cappelli, "Polarizable
- ⁶¹T. Giovannini, A. Puglisi, M. Ambrosetti, and C. Cappelli, "Polarizable QM/MM approach with fluctuating charges and fluctuating dipoles: The QM/FQFμ model," J. Chem. Theory Comput. **15**, 2233–2245 (2019).
- ⁶²T. Giovannini, R. R. Riso, M. Ambrosetti, A. Puglisi, and C. Cappelli, "Electronic transitions for a fully polarizable QM/MM approach based on fluctuating charges and fluctuating dipoles: Linear and corrected linear response regimes," J. Chem. Phys. 151, 174104 (2019).
- ⁶³ W. Liang, Z. Pei, Y. Mao, and Y. Shao, "Evaluation of molecular photophysical and photochemical properties using linear response time-dependent density functional theory with classical embedding: Successes and challenges," J. Chem. Phys. 156, 210901 (2022).
- ⁶⁴ M. J. Frisch, Y. Yamaguchi, J. F. Gaw, H. F. Schaefer, and J. S. Binkley, "Analytic Raman intensities from molecular electronic wave functions," J. Chem. Phys. 84, 531–532 (1986).
- ⁶⁵M. Frisch, M. Head-Gordon, and J. Pople, "Direct analytic SCF second derivatives and electric field properties," Chem. Phys. 141, 189–196 (1990).
- ⁶⁶O. Quinet and B. Champagne, "Time-dependent Hartree-Fock schemes for analytical evaluation of the Raman intensities," J. Chem. Phys. 115, 6293–6299 (2001).
- ⁶⁷T. Giovannini, L. Grazioli, M. Ambrosetti, and C. Cappelli, "Calculation of IR spectra with a fully polarizable QM/MM approach based on fluctuating charges and fluctuating dipoles," J. Chem. Theory Comput. **15**, 5495–5507 (2019).
- ⁶⁸T. Giovannini, M. Olszówka, F. Egidi, J. R. Cheeseman, G. Scalmani, and C. Cappelli, "Polarizable embedding approach for the analytical calculation of Raman and Raman optical activity spectra of solvated systems," J. Chem. Theory Comput. 13, 4421–4435 (2017).
- ⁶⁹ K. O. H. M. Dundas, M. T. P. Beerepoot, M. Ringholm, S. Reine, R. Bast, N. H. List, J. Kongsted, K. Ruud, and J. M. H. Olsen, "Harmonic infrared and Raman spectra in molecular environments using the polarizable embedding model," J. Chem. Theory Comput. 17, 3599–3617 (2021).
- ⁷⁰ F. Liu, Z. Gan, Y. Shao, C.-P. Hsu, A. Dreuw, M. Head-Gordon, B. T. Miller, B. R. Brooks, J.-G. Yu, T. R. Furlani, and J. Kong, "A parallel implementation of the analytic nuclear gradient for time-dependent density functional theory within the Tamm–Dancoff approximation," Mol. Phys. **108**, 2791–2800 (2010).

- ⁷¹ E. B. Wilson, J. C. Decius, and P. C. Cross, Molecular Vibrations: The Theory of Infrared and Raman Vibrational Spectra (Courier Corporation, 1980).
- ⁷²D. Porezag and M. R. Pederson, "Infrared intensities and Raman-scattering activities within density-functional theory," Phys. Rev. B **54**, 7830–7836 (1996).
- ⁷³F. Furche, "On the density matrix based approach to time-dependent density functional response theory," J. Chem. Phys. 114, 5982–5992 (2001).
- ⁷⁴S. M. Parker, D. Rappoport, and F. Furche, "Quadratic response properties from TDDFT: Trials and tribulations," J. Chem. Theory Comput. 14, 807–819 (2017).
- ⁷⁵E. Epifanovsky, A. T. B. Gilbert, X. Feng, J. Lee, Y. Mao, N. Mardirossian, P. Pokhilko, A. F. White, M. P. Coons, A. L. Dempwolff, Z. Gan, D. Hait, P. R. Horn, L. D. Jacobson, I. Kaliman, J. Kussmann, A. W. Lange, K. U. Lao, D. S. Levine, J. Liu, S. C. McKenzie, A. F. Morrison, K. D. Nanda, F. Plasser, D. R. Rehn, M. L. Vidal, Z.-Q. You, Y. Zhu, B. Alam, B. J. Albrecht, A. Aldossary, E. Alguire, J. H. Andersen, V. Athavale, D. Barton, K. Begam, A. Behn, N. Bellonzi, Y. A. Bernard, E. J. Berquist, H. G. A. Burton, A. Carreras, K. Carter-Fenk, R. Chakraborty, A. D. Chien, K. D. Closser, V. Cofer-Shabica, S. Dasgupta, M. de Wergifosse, J. Deng, M. Diedenhofen, H. Do, S. Ehlert, P.-T. Fang, S. Fatehi, Q. Feng, T. Friedhoff, J. Gayvert, Q. Ge, G. Gidofalvi, M. Goldey, J. Gomes, C. E. González-Espinoza, S. Gulania, A. O. Gunina, M. W. D. Hanson-Heine, P. H. P. Harbach, A. Hauser, M. F. Herbst, M. Hernández Vera, M. Hodecker, Z. C. Holden, S. Houck, X. Huang, K. Hui, B. C. Huynh, M. Ivanov, Á. Jász, H. Ji, H. Jiang, B. Kaduk, S. Kähler, K. Khistyaev, J. Kim, G. Kis, P. Klunzinger, Z. Koczor-Benda, J. H. Koh, D. Kosenkov, L. Koulias, T. Kowalczyk, C. M. Krauter, K. Kue, A. Kunitsa, T. Kus, I. Ladjánszki, A. Landau, K. V. Lawler, D. Lefrancois, S. Lehtola, R. R. Li, Y.-P. Li, J. Liang, M. Liebenthal, H.-H. Lin, Y.-S. Lin, F. Liu, K.-Y. Liu, M. Loipersberger, A. Luenser, A. Manjanath, P. Manohar, E. Mansoor, S. F. Manzer, S.-P. Mao, A. V. Marenich, T. Markovich, S. Mason, S. A. Maurer, P. F. McLaughlin, M. F. S. J. Menger, J.-M. Mewes, S. A. Mewes, P. Morgante, J. W. Mullinax, K. J. Oosterbaan, G. Paran, A. C. Paul, S. K. Paul, F. Pavošević, Z. Pei, S. Prager, E. I. Proynov, Á. Rák, E. Ramos-Cordoba, B. Rana, A. E. Rask, A. Rettig, R. M. Richard, F. Rob, E. Rossomme, T. Scheele, M. Scheurer, M. Schneider, N. Sergueev, S. M. Sharada, W. Skomorowski, D. W. Small, C. J. Stein, Y.-C. Su, E. J. Sundstrom, Z. Tao, J. Thirman, G. J. Tornai, T. Tsuchimochi, N. M. Tubman, S. P. Veccham, O. Vydrov, J. Wenzel, J. Witte, A. Yamada, K. Yao, S. Yeganeh, S. R. Yost, A. Zech, I. Y. Zhang, X. Zhang, Y. Zhang, D. Zuev, A. Aspuru-Guzik, A. T. Bell, N. A. Besley, K. B. Bravaya, B. R. Brooks, D. Casanova, J.-D. Chai, S. Coriani, C. J. Cramer, G. Cserey, A. E. DePrince, R. A. DiStasio, A. Dreuw, B. D. Dunietz, T. R. Furlani, W. A. Goddard, S. Hammes-Schiffer, T. Head-Gordon, W. J. Hehre, C.-P. Hsu, T.-C. Jagau, Y. Jung, A. Klamt, J. Kong, D. S. Lambrecht, W. Liang, N. J. Mayhall, C. W. McCurdy, J. B. Neaton, C. Ochsenfeld, J. A. Parkhill, R. Peverati, V. A. Rassolov, Y. Shao, L. V. Slipchenko, T. Stauch, R. P. Steele, J. E. Subotnik, A. J. W. Thom, A. Tkatchenko, D. G. Truhlar, T. Van Voorhis, T. A. Wesolowski, K. B. Whaley, H. L. Woodcock, P. M. Zimmerman, S. Faraji, P. M. W. Gill, M. Head-Gordon, J. M. Herbert, and A. I. Krylov, "Software for the frontiers of quantum chemistry: An overview of developments in the Q-Chem 5 package," J. Chem. Phys. 155, 084801 (2021).
- ⁷⁶S.-W. Joo, "Surface-enhanced Raman scattering of 4,4'-bipyridine on gold nanoparticle surfaces," Vib. Spectrosc. **34**, 269–272 (2004).
- ⁷⁷S. W. Joo, "Adsorption of bipyridine compounds on gold nanoparticle surfaces investigated by UV-vis absorbance spectroscopy and surface enhanced Raman scattering," Spectrosc. Lett. 39, 85–96 (2006).
- ⁷⁸Z. Zhuang, J. Cheng, X. Wang, B. Zhao, X. Han, and Y. Luo, "Surface-enhanced Raman spectroscopy and density functional theory study on 4,4'-bipyridine molecule," Spectrochim. Acta, Part A 67, 509–516 (2007).
- ⁷⁹Z. Zhuang, W. Ruan, N. Ji, X. Shang, X. Wang, and B. Zhao, "Surface-enhanced Raman scattering of 4,4'-bipyridine on silver by density functional theory calculations," Vib. Spectrosc. 49, 118–123 (2009).
- ⁸⁰P. M. W. Gill, B. G. Johnson, and J. A. Pople, "A standard grid for density functional calculations," Chem. Phys. Lett. 209, 506–512 (1993).
- ⁸¹ J. Neugebauer, M. Reiher, C. Kind, and B. A. Hess, "Quantum chemical calculation of vibrational spectra of large molecules—Raman and IR spectra for buckminsterfullerene," J. Comput. Chem. 23, 895–910 (2002).
- ⁸²M. D. Williams, D. S. Bradshaw, and D. L. Andrews, "Raman scattering mediated by neighboring molecules," J. Chem. Phys. 144, 174304 (2016).
- ⁸³ M. D. Williams, D. S. Bradshaw, and D. L. Andrews, "Symmetry analysis of Raman scattering mediated by neighboring molecules," J. Chem. Phys. 145, 184301 (2016).

- ⁸⁴I. Russier-Antoine, F. Bertorelle, M. Vojkovic, D. Rayane, E. Salmon, C. Jonin, P. Dugourd, R. Antoine, and P.-F. Brevet, "Non-linear optical properties of gold quantum clusters. The smaller the better," Nanoscale 6, 13572–13578 (2014).
- ⁸⁵ K. Wu, J. Li, and C. Lin, "Remarkable second-order optical nonlinearity of nanosized Au₂₀ cluster: A TDDFT study," Chem. Phys. Lett. 388, 353–357 (2004).
- ⁸⁶ R. S. Mulliken, "Electronic population analysis on LCAO–MO molecular wave functions. I," J. Chem. Phys. 23, 1833–1840 (1955).
- ⁸⁷C. M. Breneman and K. B. Wiberg, "Determining atom-centered monopoles from molecular electrostatic potentials. The need for high sampling density in formamide conformational analysis," J. Comput. Chem. 11, 361–373 (1990).
- ⁸⁸F. A. Momany, "Determination of partial atomic charges from ab initio molecular electrostatic potentials. Application to formamide, methanol, and formic acid," J. Phys. Chem. **82**, 592–601 (1978).

- ⁸⁹ J. Řezáč and A. de la Lande, "Robust, basis-set independent method for the evaluation of charge-transfer energy in noncovalent complexes," J. Chem. Theory Comput. 11, 528–537 (2015).
- ⁹⁰G. S. Kedziora and G. C. Schatz, "Calculating dipole and quadrupole polarizabilities relevant to surface enhanced Raman spectroscopy," Spectrochim. Acta, Part A 55, 625–638 (1999).
- ⁹¹ J. Yang, Z. Pei, J. Deng, Y. Mao, Q. Wu, Z. Yang, B. Wang, C. M. Aikens, W. Liang, and Y. Shao, "Analysis and visualization of energy densities. I. Insights from real-time time-dependent density functional theory simulations," Phys. Chem. Chem. Phys. 22, 26838–26851 (2020).
- ⁹²N. C. Handy and H. F. Schaefer, "On the evaluation of analytic energy derivatives for correlated wave functions," J. Chem. Phys. 81, 5031–5033 (1984).
- ⁹³D. Rappoport and F. Furche, "Lagrangian approach to molecular vibrational Raman intensities using time-dependent hybrid density functional theory," J. Chem. Phys. **126**, 201104 (2007).